# REPORT DOCUMENTATION PAGE

AFRL-SR-AR-TR-02-

0278

| 1. AGENCY USE ONLY (Leave blank) | 2. REPORT DATE 07/30/02 | 3. REPORT TYPE AND DATES COVERED Final Technical (11/15/99 – 11/14/01) |
|---|---|---|

| 4. TITLE AND SUBTITLE | 5. FUNDING NUMBERS |
|---|---|
| Numerical Investigation of the Control of Separation from Curved and Blunt Trailing Edges Using DNS and LES | F49620-00-1-0069 |

**6. AUTHOR(S)**
Professor Hermann F. Fasel

**7. PERFORMING ORGANIZATION NAME(S) AND ADDRESS(ES)**

Aerospace and Mechanical Engineering
The College of Engineering and Mines
University of Arizona
Tucson, AZ 85721

**8. PERFORMING ORGANIZATION REPORT NUMBER**

**9. SPONSORING / MONITORING AGENCY NAME(S) AND ADDRESS(ES)**

AFOSR/NA
801 N. Randolph Street
Arlington, VA 22203-1977

**10. SPONSORING / MONITORING AGENCY REPORT NUMBER**

**11. SUPPLEMENTARY NOTES**

**12a. DISTRIBUTION / AVAILABILITY STATEMENT**
Approved for Public Release
Distribution is Unlimited

20020909 138

**13. ABSTRACT (Maximum 200 Words)**
Wall jets over a curved wall geometry (Coanda flows) are investigated using DNS and turbulence modeling. In experiments large coherent structures have enhanced the effectiveness of wall jets in delaying or preventing flow separation on airfoils. Understanding the behavior of these structures is essential for utilizing wall jets for separation control. The research objective is to investigate curvature effects on large coherent structures, in particular the development of longitudinal (Goertler-type) vortices and their interaction with 2D vortices. The focus is on Coanda cylinders using two computational approaches. With the Flow Simulation Methodology (FSM), a turbulent wall jet is computed over a cylinder segment on a body-fitted grid. In FSM, the contribution of the turbulence model depends on the grid resolution relative to a local turbulent length scale. For a flat-plate reference case, FSM is employed as DNS, LES, and URANS. In all cases the large 2D vortices are captured. For the curved-wall geometry, FSM is employed as a DNS. Goertler-type vortices emerge in the simulation but remain weak due to the narrow computational domain. In the second approach, Coanda flows including nozzle and separated region are computed using immersed boundary techniques (IBT). The feasibility of IBT for Coanda Flows is established.

| 14. SUBJECT TERMS | 15. NUMBER OF PAGES 63 |
|---|---|
| | 16. PRICE CODE |

| 17. SECURITY CLASSIFICATION OF REPORT UNCLASSIFIED | 18. SECURITY CLASSIFICATION OF THIS PAGE UNCLASSIFIED | 19. SECURITY CLASSIFICATION OF ABSTRACT UNCLASSIFIED | 20. LIMITATION OF ABSTRACT UNLIMITED |
|---|---|---|---|

# NUMERICAL INVESTIGATION OF THE CONTROL OF SEPARATION FROM CURVED AND BLUNT TRAILING EDGES USING DNS AND LES

## AFOSR Grant Number F49620-00-1-0069
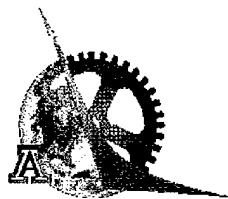
### Final Report

by

**Hermann F. Fasel** and **Stefan Wernz**

Department of Aerospace and Mechanical Engineering

The University of Arizona

Tucson, AZ 85721

Submitted to

The Air Force Office of Scientific Research

February 2002

## Abstract

In a numerical effort, wall jets over a curved wall geometry (Coanda flows) have been investigated using Direct Numerical Simulation (DNS) and a new turbulence modeling approach. The present research is motivated by experimental results indicating that the presence of large coherent structures can greatly enhance the effectiveness of wall jets in delaying or preventing flow separation on airfoils. For utilizing wall jets as separation control devices to their full potential a deeper understanding of the generation and development of these large structures is essential. The objective of the present research has been to investigate the effect of curvature on the development of large coherent structures in wall jets, in particular the development of longitudinal vortices (Görtler type) and their interaction with two-dimensional vortical structures. The focus has been on Coanda flows over circular cylinders using two different computational approaches. In the first approach, the new Flow Simulation Methodology (FSM) was employed on a body-fitted grid to compute a turbulent wall jet over a segment of the Coanda cylinder. In FSM, the contribution of the turbulence model is ramped in depending on the grid resolution relative to the local Kolmogorov length scale. The turbulent flow was generated through a bypass-type transition triggered by three-dimensional, large amplitude forcing of a laminar wall jet. For the flat plate reference case, FSM was employed as a DNS, LES and in the URANS limit. In all these cases FSM was able to capture the large two-dimensional vortical structures. For the curved wall geometry, FSM has been employed thus far only in the DNS limit. While Görtler type 3D vortices are observed in the DNS, they remain very weak compared with the 2D structures. This was probably due to the relatively narrow computational domain chosen for the simulations. In the second approach, the complete Coanda flow including the nozzle was computed using an immersed boundary technique (IBT). This approach includes effects of the nozzle geometry and any global effects of the flow separation. With 2D simulations the feasibility of IBT for computing Coanda flows was established. Trends for the dependence of the separation location on the Reynolds number measured in experiments were confirmed with our numerical investigations.

# Contents

# 1 Introduction

Extensive experimental research by Wygnanski and co-workers (Wygnanski 1997) has provided considerable evidence that periodically forced wall jets (tangential oscillatory blowing) may be an effective method for the control of separation of flows over single-element or segmented airfoils (including flaps). The setup of two such experiments is illustrated in Figure 1. In the experiment by Seifert et al. (1994), a high momentum jet that is blown through the slot along the upper surface of the flap is periodically forced at the location indicated in Figure 1a. The additional forcing strongly improves the effectiveness of the weak wall jet in preventing separation, and thus allows for significantly higher angles of attack. In the experiments by Seifert et al. (1993) on an airfoil with a straight flap, lift increase could be maximized with the combination of weak steady blowing and relatively low momentum oscillations. Coherent structures generated by the forcing eliminated the large wake region that was present above the wall jet when only steady blowing was used through surface-normal transport of momentum.

While the effectiveness of pulsed blowing for separation control was clearly established with the experiments, many of the fundamental instability mechanisms that are responsible for preventing or delaying flow separation in the forced flow are still
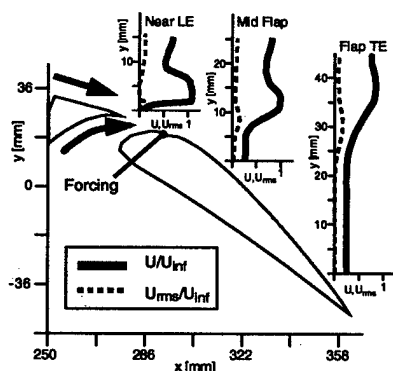
a) Experiment by Seifert et al. (1994)
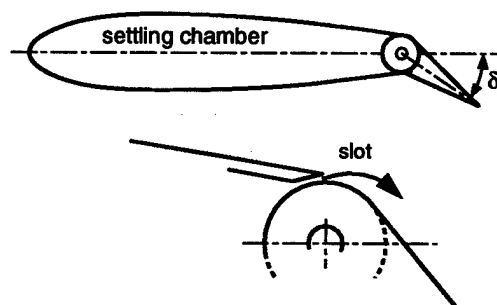
b) NACA 0015 airfoil with slotted flap from experiments by Seifert et al. (1993)

Figure 1: Experiments on active separation control by Wygnanski and coworkers.

not understood. For example, experiments have shown that wall curvature, both convex and concave, as well as tangential blowing (or local suction), may have a puzzling effect on the effectiveness of periodic excitation; in certain instances the effect of periodic excitation may be enhanced while in other situations it can be diminished. Understanding the behavior of the large coherent structures and their control for flow separation on airfoils is extremely difficult due to the great complexity of the complete airfoil flow geometry which is influenced by many parameters; e.g., adverse pressure gradient, curvature, jet momentum, nozzle geometry, forcing method. For gaining insight into the major contributing instability mechanisms we investigated prototypical flow geometries that include some but not all aspects of the airfoil geometry. In previously funded research (AFOSR GRANT F49620-97-1-0274) the effect of curvature was excluded by focusing on pulsed wall jets injected into separating flat-plate boundary layers. In the present research project we have investigated curvature effects on wall jets separately by studying prototypical wall jets over curved surfaces, specifically Coanda flows where fluid is blown tangentially along a cylinder surface. and, due to a surface-normal pressure gradient, adheres to the curved surface over relatively large downstream distances.

As illustrated with the schematic in Figure 2 a jet is issued from the nozzle at angle $\theta_0$ and develops along the cylinder surface as a so called Coanda flow. The Coanda
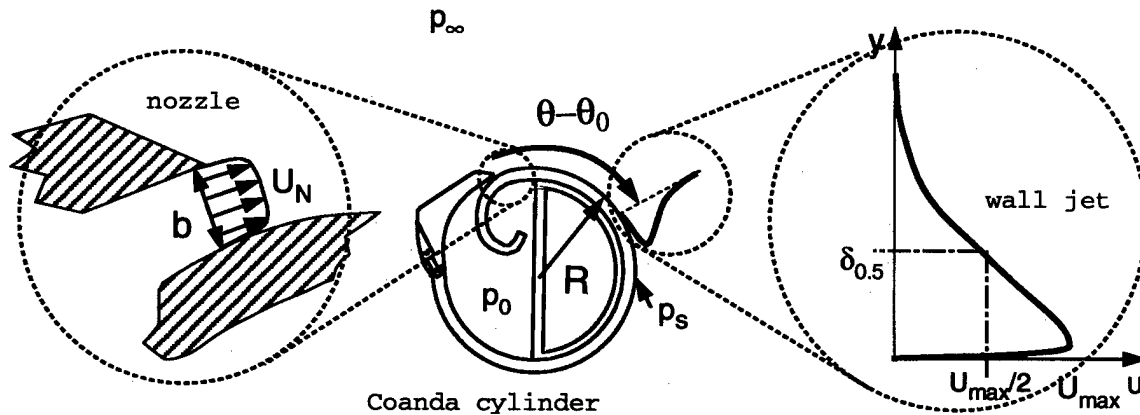


Figure 2: Important flow parameters for the Coanda flow.

flow adheres to the cylinder because of a pressure difference between the ambient pressure, $p_\infty$, and a lower pressure at the surface, $p_s$, which builds due to streamline curvature and can be computed from the surface-normal momentum balance,

$$p_\infty - p_s = \rho \int_0^\infty \frac{\bar{u}^2 + \overline{u'^2}}{R + r} dr \,.$$

(1)

In the experiments of a turbulent Coanda flow by Neuendorf and Wygnanski (1999) (experimental setup shown in Figure 3a), the jet remains attached for about $\theta - \theta_0 = 210°$. Through nondimensionalization, the surface pressure coefficient is defined as

$$c_p = \frac{(p_\infty - p_s)R}{(p_0 - p_\infty)b} = \ldots = f(\theta - \theta_0, Re_N) \,,$$

(2)

which depends on the distance from the nozzle and a so-called "nominal Reynolds number" defined by Newman (1961),

$$Re_N = \sqrt{\frac{(p_0 - p_\infty)bR}{\rho\nu^2}} \,.$$

(3)

With the following definition of the jet exit momentum assuming a top hat profile at the nozzle,

$$J_N \equiv U_N^2 \cdot b \approx \frac{2b}{\rho}(p_0 - p_\infty) \,,$$

(4)

the nominal Reynolds number can also be written as

$$Re_N \approx \sqrt{\frac{J_N R}{2\nu^2}} = \frac{1}{2}\sqrt{Re_D \cdot Re_b} \,,$$

(5)

which is the geometric mean of two Reynolds numbers based on cylinder diameter, $D$, and on nozzle width, $b$, respectively.

Due to streamline curvature the Coanda flow can be susceptible to a centrifugal instability that leads to Görtler-type streamwise vortices. This instability depends on another modified Reynolds number, the Görtler number

$$G\ddot{o} = Re_{\delta 0.5}\sqrt{\delta_{0.5}/R}, \qquad \text{where} \quad Re_{\delta 0.5} = U_{max}\delta_{0.5}/\nu$$

(6)

with the local velocity maximum $U_{max}$ and the half width $\delta_{0.5}$ of the streamwise velocity profile of the wall jet. In the experiments by Neuendorf (2000) (Figure 3a),
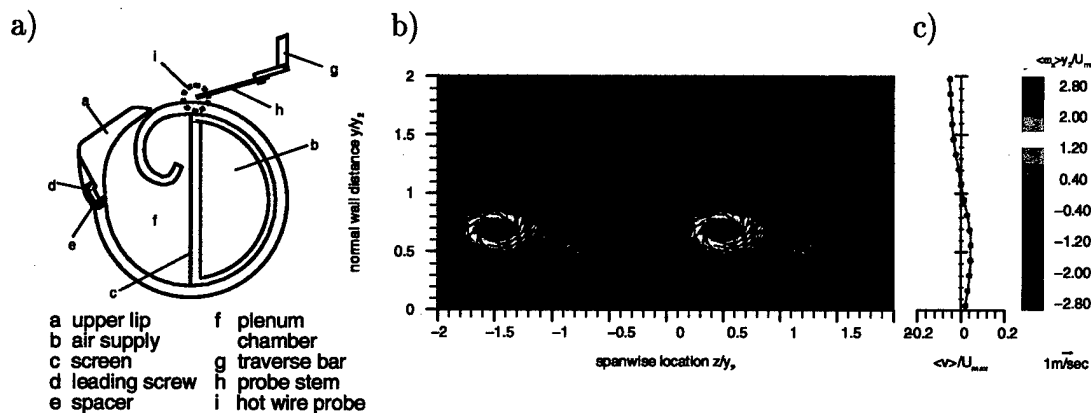
Figure 3: From experiments by Neuendorf (2000) on the Coanda flow: a) experimental setup, b) contours of phase averaged streamwise vorticity, and c) profile of the spanwise averaged radial velocity at $\theta = 80°$ from the nozzle.

it was convincingly shown that longitudinal vortices of the Görtler type arise in the shear layer of the outer flow region (Figure 3b,c) by virtue of a centrifugal instability mechanism and grow in size and strength in streamwise direction. This 3-D mechanism may compete and interact with the 2-D instability mechanism of the outer shear layer and therefore reduce the effect of any 2-D periodic forcing.

The main focus of the present research has been to capture and investigate the dynamics of the 2-D and 3-D large coherent structures. Two computational avenues have been pursued to achieve this goal. In the first approach, the flow is computed on a body-fitted grid using an incompressible Navier-Stokes code which was originally developed for Direct Numerical Simulation (DNS) of transition in various flows over flat-plate geometries (boundary layers, plane wall jets) and which has been extended to curved wall geometries (Zhang and Fasel 1999). With this code we were able to perform Direct Numerical Simulations of a plane turbulent wall jet which serves as a reference (section 4.1) and of the flow over a segment of the Coanda cylinder (section 4.2). In order to relax the resolution requirements for computing turbulent flows a new turbulence modeling approach has been developed in our group over the past few years, originally in cooperation with C. Speziale of Boston University (see

Speziale 1998). This so called Flow Simulation Methodology (FSM) is designed to be consistent with DNS for a fine grid resolution and with unsteady RANS for a coarse grid resolution, and represents an LES between those limits. As discussed in section 4.3 we could demonstrate the capability of FSM to capture large coherent structures in wall jet flows for the whole range of application from DNS over LES to URANS. Simulation of the whole Coanda flow geometry including the nozzle and the separated flow region is, however, beyond the current computational approach on a body-fitted grid. Therefore, a Cartesian grid method using immersed boundary techniques (IBT) for representing solid bodies inside the computational domain has been employed to compute the whole flow field around a Coanda cylinder. Results from selected test calculations of this novel approach are presented in section 5.1 and a discussion of results for the Coanda flow is provided in section 5.2.

# 2  Computational Method — Body Fitted Grid

The Navier-Stokes code employed for our numerical investigations on the body fitted grid was originally developed in our research group for boundary layer transition (see Meitz and Fasel, 2000) and has since been adapted to the wall jet flow geometry.

## 2.1  Governing Equations

In our code, the complete incompressible Navier-Stokes equations are solved in vorticity-velocity formulation. Regardless of which form of time averaging or spatial filtering is applied, the resulting transport equations take on the form,

$$\frac{\partial \overline{\omega}}{\partial t} + \nabla \times \left( \overline{\omega} \times \overline{V} - \nabla \cdot \vec{\vec{\tau}} \right) = \frac{1}{Re} \nabla^2 \overline{\omega}. \qquad (7)$$

The overbar on the velocity vector $\vec{V}$ and on the vorticity vector $\vec{\omega}$ denotes the operation of averaging the appropriate components of the corresponding vector. For simplicity, overbars are omitted from now on in this report. The quantity $\vec{\vec{\tau}} = [\tau_{ij}]$ is the turbulent stress tensor which must be modeled. Equation (7) is non-dimensionalized by the free-stream velocity $U_\infty$, a reference length $L$, and a global Reynolds number defined as $Re = U_\infty L / \nu$ where $\nu$ is the kinematic viscosity.

For the present calculations of the Coanda flow a simplified curvilinear grid is used. As shown in Figure 4, the computational domain wraps around the cylinder surface with a constant domain height. The grid coordinates are defined as follows:

$$x = x_0(s) - \eta \sin \theta(s), \qquad (8)$$

$$y = y_0(s) + r \cos \theta(s), \qquad (9)$$

where $s$ is the arc length on the surface, $x_0(s)$ and $y_0(s)$ are the surface coordinates, and $r$ is the normal distance from the surface. This simplified curvilinear grid has properties that enables us to retain much of the highly efficient and accurate numerical scheme employed by the original code in Cartesian coordinates. The grid is
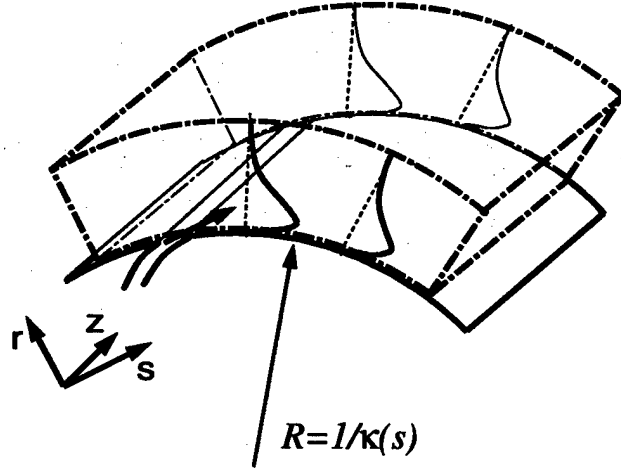
$R=1/\kappa(s)$

Figure 4: Schematic of the computational grid for Coanda flow computations using a body-fitted grid .

orthogonal,

$$\frac{\partial x}{\partial s}\frac{\partial x}{\partial r} + \frac{\partial y}{\partial s}\frac{\partial y}{\partial r} = 0, \tag{10}$$

and the resulting metric coefficients are

$$h_1 \equiv h = \sqrt{\left(\frac{\partial x}{\partial s}\right)^2 + \left(\frac{\partial y}{\partial s}\right)^2} = (1 - r\kappa(s)), \tag{11}$$

where $\kappa(s)$ is the the curvature of the surface, with $\kappa(s) > 0$ for concave wall and $\kappa(s) < 0$ for convex wall, respectively. Note, $h_2 = h_3 = 1$.

In these curvilinear coordinates the vorticity transport equations then write as

$$\frac{\partial \omega_s}{\partial t} + \frac{\partial}{\partial r}(\omega_s v - \omega_r u) - \frac{\partial}{\partial z}(\omega_z u - \omega_s w)$$
$$= \nu \left\{ \nabla^2 \omega_s - \frac{2\kappa(s)}{h^2}\frac{\partial \omega_r}{\partial s} - \omega_s \left[\frac{\kappa^2(s)}{h^2}\right] - \omega_r \left[\frac{r\kappa(s)\kappa'(s)}{h^3} + \frac{\kappa'(s)}{h^2}\right] \right\}, \tag{12}$$

$$\frac{\partial \omega_r}{\partial t} + \frac{\partial}{\partial z}(\omega_r w - \omega_z v) - \frac{1}{h}\frac{\partial}{\partial s}(\omega_s v - \omega_r u)$$
$$= \nu \left\{ \nabla^2 \omega_r + \frac{2\kappa(s)}{h^2}\frac{\partial \omega_s}{\partial s} - \omega_r \left[\frac{\kappa^2(s)}{h^2}\right] + \omega_s \left[\frac{r\kappa(s)\kappa'(s)}{h^3} + \frac{\kappa'(s)}{h^2}\right] \right\}, \tag{13}$$

$$\frac{\partial \omega_z}{\partial t} + \frac{1}{h}\frac{\partial}{\partial s}(\omega_z u - \omega_s w) - \frac{1}{h}\frac{\partial}{\partial r}[h(\omega_r w - \omega_z v)] = \nu \nabla^2 \omega_z, \tag{14}$$

where

$$\nabla^2 = \frac{1}{h}\frac{\partial}{\partial s}\left(\frac{1}{h}\frac{\partial}{\partial s}\right) + \frac{1}{h}\frac{\partial}{\partial r}\left(h\frac{\partial}{\partial r}\right) + \frac{\partial^2}{\partial z^2}$$

$$= \frac{r\kappa'(s)}{h^3}\frac{\partial}{\partial s} + \frac{1}{h^2}\frac{\partial^2}{\partial s^2} - \frac{\kappa(s)}{h}\frac{\partial}{\partial r} + \frac{\partial^2}{\partial r^2} + \frac{\partial^2}{\partial z^2}. \tag{15}$$

The vorticity components are defined as

$$\omega_s = -\left(\frac{\partial w}{\partial r} - \frac{\partial v}{\partial z}\right), \tag{16}$$

$$\omega_r = -\left(\frac{\partial u}{\partial z} - \frac{1}{h}\frac{\partial w}{\partial s}\right), \tag{17}$$

$$\omega_z = -\left(\frac{1}{h}\frac{\partial v}{\partial s} - \frac{\partial u}{\partial r} + \frac{u\kappa(s)}{h}\right). \tag{18}$$

In addition to the vorticity transport equations, the following Poisson equations are solved to obtain the velocity field in curvilinear coordinates:

$$\frac{\partial^2 v}{\partial s^2} + \frac{\partial^2 v}{\partial r^2} + \frac{\partial^2 v}{\partial z^2} = -\frac{\partial(h\omega_z)}{\partial s} + \frac{\partial\omega_s}{\partial z} + \frac{\partial}{\partial r}\left(\frac{\partial hu}{\partial s} - \frac{1}{h}\frac{\partial u}{\partial s} + \frac{v\kappa(s)}{h}\right), \tag{19}$$

$$\frac{1}{h}\frac{\partial}{\partial s}\left(\frac{1}{h}\frac{\partial u}{\partial s}\right) + \frac{\partial^2 u}{\partial z^2} = -\frac{\partial\omega_r}{\partial z} - \frac{1}{h}\frac{\partial}{\partial s}\left(\frac{1}{h}\frac{\partial hv}{\partial r}\right), \tag{20}$$

$$\frac{1}{h}\frac{\partial}{\partial s}\left(\frac{1}{h}\frac{\partial w}{\partial s}\right) + \frac{\partial^2 w}{\partial z^2} = \frac{1}{h}\frac{\partial\omega_r}{\partial s} - \frac{\partial}{\partial z}\left(\frac{1}{h}\frac{\partial hv}{\partial r}\right). \tag{21}$$

The wall vorticity is calculated from the velocities to ensure zero–divergence of the vorticity:

$$\frac{\partial^2\omega_s}{\partial s^2} + \frac{\partial^2\omega_s}{\partial z^2} = -\frac{\partial^2 h\omega_r}{\partial s\partial r} + \frac{\partial}{\partial z}\left(\frac{\partial^2 v}{\partial s^2} + \frac{\partial^2 v}{\partial r^2} + \frac{\partial^2 v}{\partial z^2}\right) \tag{22}$$

$$- \frac{\partial}{\partial z}\left[\frac{\partial}{\partial r}\left(\frac{\partial hu}{\partial s} - \frac{1}{h}\frac{\partial u}{\partial s} + \frac{v\kappa(s)}{h}\right)\right],$$

$$\omega_r = 0, \tag{23}$$

$$\frac{\partial(h\omega_z)}{\partial s} = \frac{\partial\omega_s}{\partial z} + \frac{\partial}{\partial r}\left(\frac{\partial hu}{\partial s} - \frac{1}{h}\frac{\partial u}{\partial s} + \frac{v\kappa(s)}{h}\right) - \left(\frac{\partial^2 v}{\partial s^2} + \frac{\partial^2 v}{\partial r^2} + \frac{\partial^2 v}{\partial z^2}\right). \tag{24}$$

## 2.2 Flow Simulation Methodology (FSM)

In our turbulent flow calculations, the turbulent stress tensor $[\tau_{ij}]$ in equation (7). is modeled using a new Flow Simulation Methodology (FSM). FSM has been developed in collaboration with C. Speziale (1998) as a turbulence modeling approach for complex turbulent flows containing large coherent structures. A key feature of this new FSM is that it is consistent with DNS for fine grid resolution and with Reynolds-Averaged Navier-Stokes (RANS) calculations for coarse grid resolution. This is achieved by modeling of the turbulent stress tensor $[\tau_{ij}]$ in equation (7) as

$$\tau_{ij} = f(\Delta/L_k)\,\tau_{ij}^R, \tag{25}$$

where $\tau_{ij}^R$ is the Reynolds stress tensor, and $f(\Delta/L_k)$ is the so-called contribution function. The terms $\Delta = [(dx^2 + dy^2 + dz^2)/3]^{1/2}$ and $L_k = \nu^{3/4}/\epsilon^{1/4}$ are the representative computational grid size and the Kolmogorov length scale, respectively. In the coarse grid limit, $f(\Delta/L_k) \to 1$, a RANS calculation is recovered. In the fine grid limit, $f(\Delta/L_k) \to 0$, the FSM approaches a Direct Numerical Simulation (DNS). For the Reynolds stress, $\tau_{ij}^R$, in equation (25), the Algebraic Stress Model (ASM) of Gatski and Speziale (1993) is used that allows for a misalignment between the stress and strain rate tensor as it occurs in non-equilibrium flows. Further details of the turbulence modeling in our FSM approach are provided in a paper[1] presented at the AIAA Aerospace Sciences Meeting in Reno (Wernz et al. 2002).

## 2.3 Numerical Scheme

A detailed review of the numerical schemes used for the solution of equation (7) and the Poisson equations for the velocities (in Cartesian coordinates) can be found in Meitz and Fasel (2000). With the simplified curvilinear coordinates, the numerical procedure required only minor extensions by including a few extra terms into the

---

[1]A copy of the paper is attached at the end of this report.

governing equation. In summary, the time dependent spatially varying flow field is calculated using the so-called spatial model (inflow–outflow). For the time integration a fourth-order accurate explicit Runge-Kutta scheme is employed. Spatial derivatives in the streamwise direction are approximated by fourth-order compact differences employing upwind biased and downwind biased switching. Wall-normal derivatives are computed with fourth-order compact differences that allow for grid stretching. Pseudo-spectral decomposition is utilized in the spanwise direction, $z$. Lastly, a fast Poisson solver (see Meitz and Fasel 2000) is implemented for solving the Poisson equations to obtain the velocity components.

## 2.4   Boundary Conditions and Disturbance Generation

For calculations on the body-fitted grid, the nozzle flow is not computed. Instead, a laminar wall jet is prescribed by imposing Dirichlet conditions at the inflow. At the wall, no-slip and no-penetration conditions are imposed. The upper boundary is assumed to lie well outside the wall jet where the flow is irrotational. Hence the vorticity components are set to zero along this boundary. Also, for the surface-normal velocity a Neumann condition is prescribed which ensures (through continuity) that the surface-parallel velocity remains zero along the upper boundary. At the outflow boundary, a buffer domain is employed for damping out the time-dependent fluctuations of the flow and thus minimizing reflections from the outflow boundary. The ramping technique is similar to that proposed by Kloker et al. (1993) and is discussed in detail by Meitz (2000). In spanwise direction, periodicity is assumed, which is automatically satisfied by the spectral treatment of this direction in the numerical scheme.

Close to the inflow, the laminar flow is tripped with a volume forcing technique which was proven very effective for plane wall jets (Wernz 2001). Two forcing blobs are placed inside the inner and outer region of the wall jet at two wall-normal locations

a) distribution of volume force     b) time signal for one spanwise Fourier mode
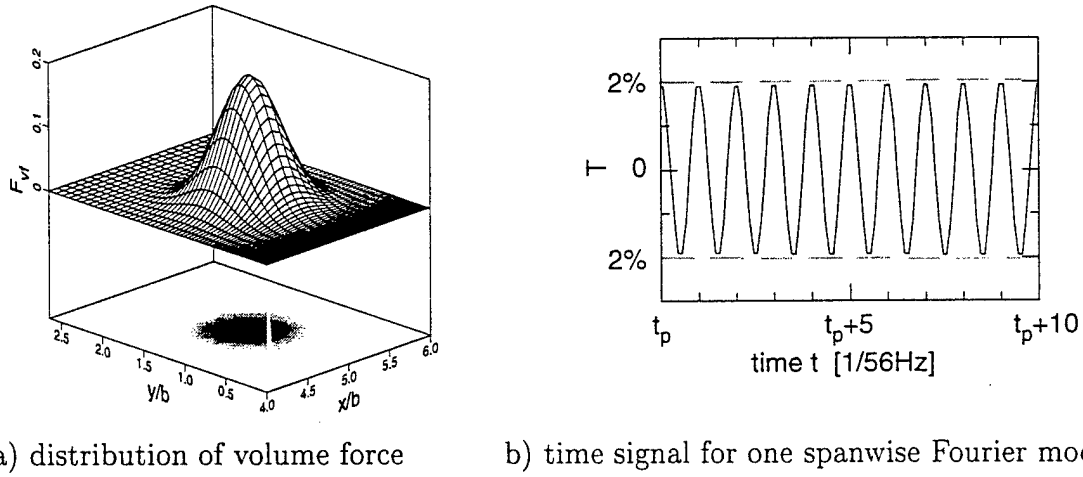
Figure 5: Disturbance generation through volume forcing.

where the flow is most receptive to disturbances. The spatial shape of these forcing blobs is illustrated in Figure 5a, 3D periodic volume forcing (in several spanwise Fourier modes) at large amplitudes (Figure 5b) and with a combination of different frequencies for each spanwise Fourier mode quickly produces a broad disturbance spectrum and leads to a rapid flow transition to turbulence.

# 3 Computational Method — Immersed Boundary Technique

The second computational approach is a Cartesian grid method using an existing compressible Navier-Stokes code developed in our group (Harris 1997). This approach provides greater flexibility for predicting flows with complex geometries and enabled us for the present research to model the Coanda cylinder from the experiments by Neuendorf and Wygnanski (1999) including the nozzle geometry. To account for solid bodies inside the computational domain immersed boundary techniques have been incorporated into the code. These techniques employ forcing terms which are added to the right-hand side of the momentum equations to enforce zero velocity at the surface of a body or throughout a solid body.

## 3.1 Governing Equations

The governing equations for the compressible code by Harris (1997) are the non-dimensionalized compressible Navier-Stokes equations in conservation form. Nondimensionalization of the governing equations is carried out by using a characteristic length scale (i.e. the cylinder diameter, $D^{*2}$), a reference velocity, temperature, density, and specific heat ($U_0^*$, $T_0^*$, $\rho_0^*$, and $C_{p0}^*$, respectively). Using these reference quantities, non-dimensional parameters are formed that characterize the compressible flow, namely the Mach number, Reynolds number, and Prandtl number,

$$Ma = \frac{U_0^*}{a_0^*} = \frac{U_0^*}{\sqrt{(\gamma - 1))C_{p0}^* T_0^*}}, \qquad Re = \frac{\rho_0^* D_0^* U_0^*}{\mu^* 0}, \qquad Pr = \mu_0^* C_{p0}^* \kappa_0^*. \qquad (26)$$

The non-dimensionalized governing equations (continuity, momentum and energy equations) are:

$$\frac{\partial \rho}{\partial t} + \frac{\partial}{\partial x_j}(\rho u_j) = 0, \qquad (27)$$

$$\frac{\partial \rho u_i}{\partial t} + \frac{\partial}{\partial x_j}(\rho u_i u_j + \delta_{ij} p - \tau_{ij}) = 0, \qquad (28)$$

---

[2]The asterisk denotes dimensional variables.

$$\frac{\partial E_t}{\partial t} + \frac{\partial}{\partial x_j}[(E_t + p)u_j - u_i\tau_{ij} + q_j] = 0 \,, \tag{29}$$

where the total Energy, $E_t$, the viscous stress, $\tau_{ij}$, and the heat flux, $q_i$, are defined as

$$E_t = \rho\left(\frac{T}{\gamma(\gamma - 1)Ma^2} + \frac{u_k u_k}{2}\right) \,, \tag{30}$$

$$\tau_{ij} = \frac{\mu}{Re}\left(\frac{\partial u_i}{\partial x_j} + \frac{\partial u_j}{\partial x_i} - \frac{2}{3}\delta_{ij}\frac{\partial u_k}{\partial x_k}\right) \,, \tag{31}$$

$$q_i = -\frac{\mu}{(\gamma - 1)Ma^2 RePr}\frac{\partial T}{\partial x_i} \,, \tag{32}$$

with $\gamma = 1.4$, and Prandtl number $Pr = 0.71$. The viscosity, $\mu$, is calculated using Sutherland's law,

$$\mu(T) = T^{2/3}\left(\frac{1 + S}{T + S}\right), \quad \text{where} \quad S = \frac{111K}{T_0^*} \,. \tag{33}$$

Lastly, the equation of state for a perfect gas is invoked to determine the pressure,

$$p = \frac{\rho T}{\gamma Ma^2}. \tag{34}$$

For the present calculations, the two-dimensional form of the compressible Navier-Stokes equations is used. In vector form, they write as

$$\frac{\partial U}{\partial t} + \frac{\partial F}{\partial x} + \frac{\partial G}{\partial y} = H + M \,, \tag{35}$$

where

$$U = \begin{bmatrix} \rho \\ \rho u \\ \rho v \\ E_t \end{bmatrix} \,,$$

$$F = \begin{bmatrix} \rho u \\ \rho u^2 + p - \tau_{xx} \\ \rho uv - \tau_{xy} \\ (E_t + p)u - u\tau_{xx} - v\tau_{xy} + q_x \end{bmatrix} \,,$$

$$G = \begin{bmatrix} \rho v \\ \rho u v - \tau_{xy} \\ \rho v^2 + p - \tau_{yy} \\ (E_t + p)v - u\tau_{xy} - v\tau_{yy} + q_y \end{bmatrix}.$$

The right hand-side terms in equation (35), H and M, represent forcing terms which are discussed in sections 3.2 and 3.3 respectively.

## 3.2   Boundary Conditions — Immersed Boundary Technique

Boundary conditions for the intergration domain shown in Figure 6 include a small uniform freestream imposed at the inflow boundary (left) and filtering inside a buffer domain at the outflow boundary (right) to damp out large vortical structures before they reach the boundary. The no-slip and no-penetration conditions along the surface of the Coanda cylinder inside the computational domain are satisfied using the immersed boundary technique. Through a forcing term, $H$, added on the right-hand side of the governing equation (35),
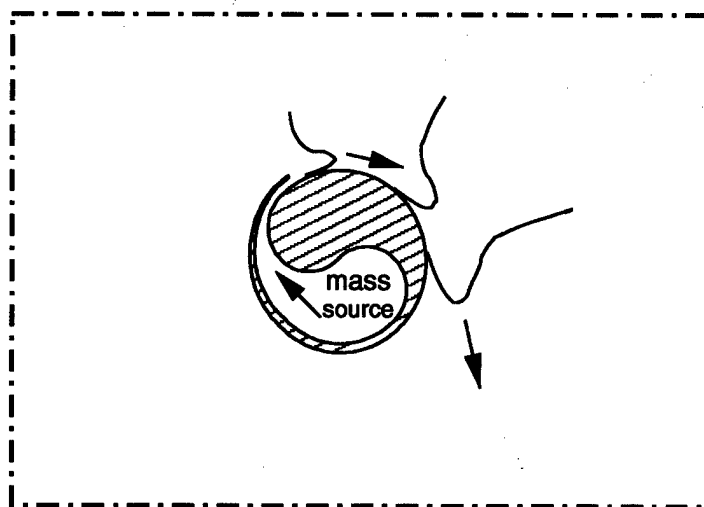


Figure 6: Schematic of the computational domain for Coanda flow computations using a Cartesian grid method.

$$H = \begin{bmatrix} 0 \\ f_x \\ f_y \\ uf_x + vf_y + g \end{bmatrix}, \qquad (36)$$

the fluid particles are brought to rest along the surface of the cylinder. For computing the components of $H$ several methods have been considered including a feed back control method proposed by Goldstein et al. (1993) and a direct method that directly sets the desired velocity values at the immersed boundary (Mohd-Yusof 1997) have been considered. More details on these techniques are provided in the paper by Terzi et al. (2001).

## 3.3 Wall Jet Generation

The wall jet is generated by placing a circular mass source into the cavity inside the Coanda cylinder (Figure 6). This is accomplished via the second forcing term on the right-hand-side of governing equation (35),

$$M = \begin{bmatrix} \dot{m} \\ 0 \\ 0 \\ \dot{h} \end{bmatrix}. \qquad (37)$$

To avoid sharp gradients in the flow field, the density flux distribution, $\dot{m}$, is represented by a Gaussian,

$$\dot{m}(r) = A_m \frac{-\ln \kappa}{\pi r_m^2} \exp(\ln \kappa (r/r_m)^2), \qquad (38)$$

where $r_m$ is the radius of the density source, $r$ the distance to its center location, $\kappa$ the value of the Gaussian at $r = r_m$ (small), and $A_m$ the total strength of the density flux. In addition, an enthalpy flux $\dot{h} = \dot{m} C_p T_m$ must be included in term $M$ to provide the added mass with a temperature, $T_m$. The mass source causes a pressure buildup inside the cylinder cavity, which accellerates the fluid through the contraction and nozzle exit and issues the wall jet along the outside surface of the cylinder (see Figure 6).
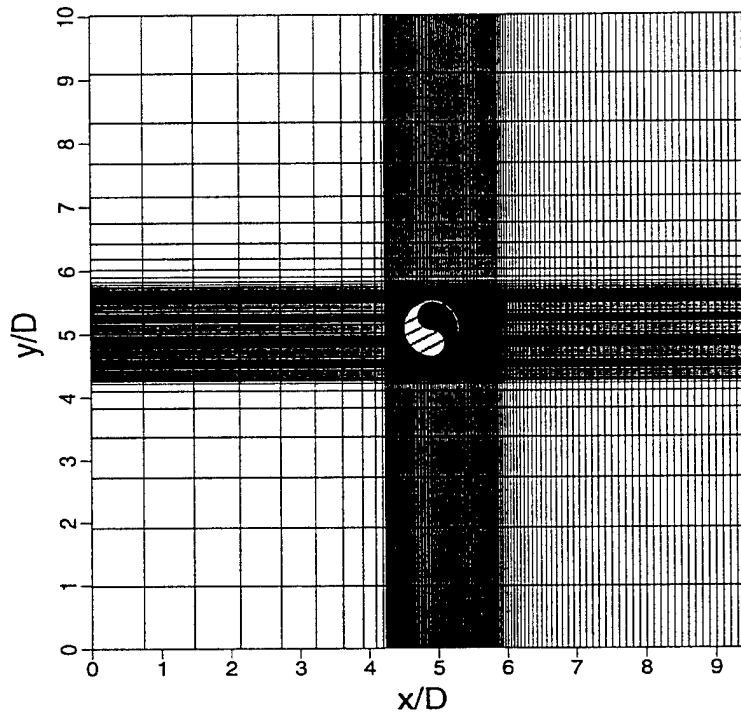
Figure 7: Example of a computational grid for Coanda flow computations using a Cartesian grid method.

## 3.4 Numerical Scheme

The compressible Navier-Stokes equations are solved using a finite-difference method. To allow for comparison with incompressible calculations, a Mach number of $Ma = 0.25$ is used. The equations are discretized using either the second-order MacCormack method (Tannehill 1997) or a fourth-order split finite-difference discretization combined with a fourth-order Runge-Kutta time integration. The latter method is described in detail by Harris (1997) and has also been used for backward-facing step flows by Terzi (1998). The numerical scheme allows for clustering of grid points in both, $x$ and $y$ directions, which allows for grid refinement near the cylinder inside the computational domain (Figure 7).

# 4    Results from the Body-Fitted Grid Calculations

The objective of our Direct Numerical Simulations of the turbulent wall jet over a curved surface is to capture the dynamics of the 2D and 3D coherent structures that develop in the flow. The DNS will then serve as a reference for computationally less expensive FSM calculations that compute the large coherent structures while modeling the effect of small scale structures with the turbulence model. In the calculations, a laminar wall jet with $Re_{\delta 0.5} = 16,500$ is transitioned to turbulence using the forcing method discussed in section 2.4. The DNS are performed on an equidistant grid with 801 points in streamwise direction, on a stretched grid in wall-normal direction with 200 points, and with 21 symmetric Fourier modes in spanwise direction. For the FSM, the resolution is reduced in the streamwise and spanwise directions.

## 4.1    DNS of Turbulent Plane Wall Jet (Reference)

As a first step, we have performed a DNS of a turbulent plane wall jet with the same domain size and resolution as used later on for the Coanda flow. Due to the strong spreading of the turbulent wall jet and the discrepancy in scale between the inner and the outer flow region, a well resolved DNS is beyond our present computational capabilities. The current coarse DNS therefore represents a compromise using a fairly narrow domain, a symmetric Fourier transform in spanwise direction (half the cost of the full transform), and a coarse wall-normal resolution in the outer flow region. Despite these shortcomings, the quality of the computed flow is surprisingly good. This is demonstrated in Figure 8 where characteristic time-averaged flow quantities from the calculation are plotted in inner and in outer coordinates at five streamwise locations and are compared with experimental measurements by Eriksson et al. (1998). Despite the short time-period for the averaging, the streamwise and wall-normal velocity profiles in Figure 8a-d are quite well converged. Except for the first and last streamwise station, which are too close to the forcing location and the buffer domain respectively, both streamwise and wall-normal velocity profiles match

the experimental data quite well in both inner and outer coordinates. The agreement is, in fact, far better than in any previous attempt at computing a fully turbulent wall jet using DNS, particularly for $y^+ < 100$ in inner coordinates. Interestingly, the streamwise velocity in Figure 8a exhibits an apparent log-layer which is much more pronounced and closer to the experimental data than for RANS calculations. The turbulent shear stress in Figures 8e&f also exhibits a very good match between DNS and experiment, particularly close to the wall where the DNS captures the near-wall asymptotic behavior.

The presence of coherent structures in the turbulent wall jet can be demonstrated with the snapshots of the flow field presented in Figure 9. Shown in Figure 9a are color contours of the spanwise average of the spanwise vorticity for the computational domain excluding the buffer at the outflow, shown in Figure 9b for the same domain are iso-surfaces of two levels of spanwise vorticity, $\omega_z = -1$ (counterclockwise rotation) and $\omega_z = 1$ (clockwise rotation). Due to the 3D forcing close to the inflow, the wall jet breaks down rapidly. Despite the purely 3D forcing, large 2D vortical structures emerge during flow transition. The structures form at $x \approx 20$ as dipolar vortex pairs, but farther downstream only the vortices with counterclockwise rotation in the outer flow region persist, while the vortices with clockwise rotation in the inner flow region have mostly disintegrated into small-scale fluctuations. This clearly indicates that the outer shear layer of the turbulent flow supports 2D vortical structures. The development in time of these structures is nicely illustrated with the space-time diagram in Figure 10a which contains the imprint onto the wall of the 2D structures inside the flow field over time (their time-traces). Shown is the spanwise averaged spanwise wall-vorticity normalized by its local time-average. While the vortices travel downstream, subsequent vortices merge and form larger sized vortices, as indicated by the merging of their time-traces in the space-time diagram.

a) streamwise velocity in inner coords.

b) streamwise velocity in outer coords.

c) wall-normal velocity in inner coords.

d) wall-normal velocity in outer coords.

e) Reynolds stress in inner coords.
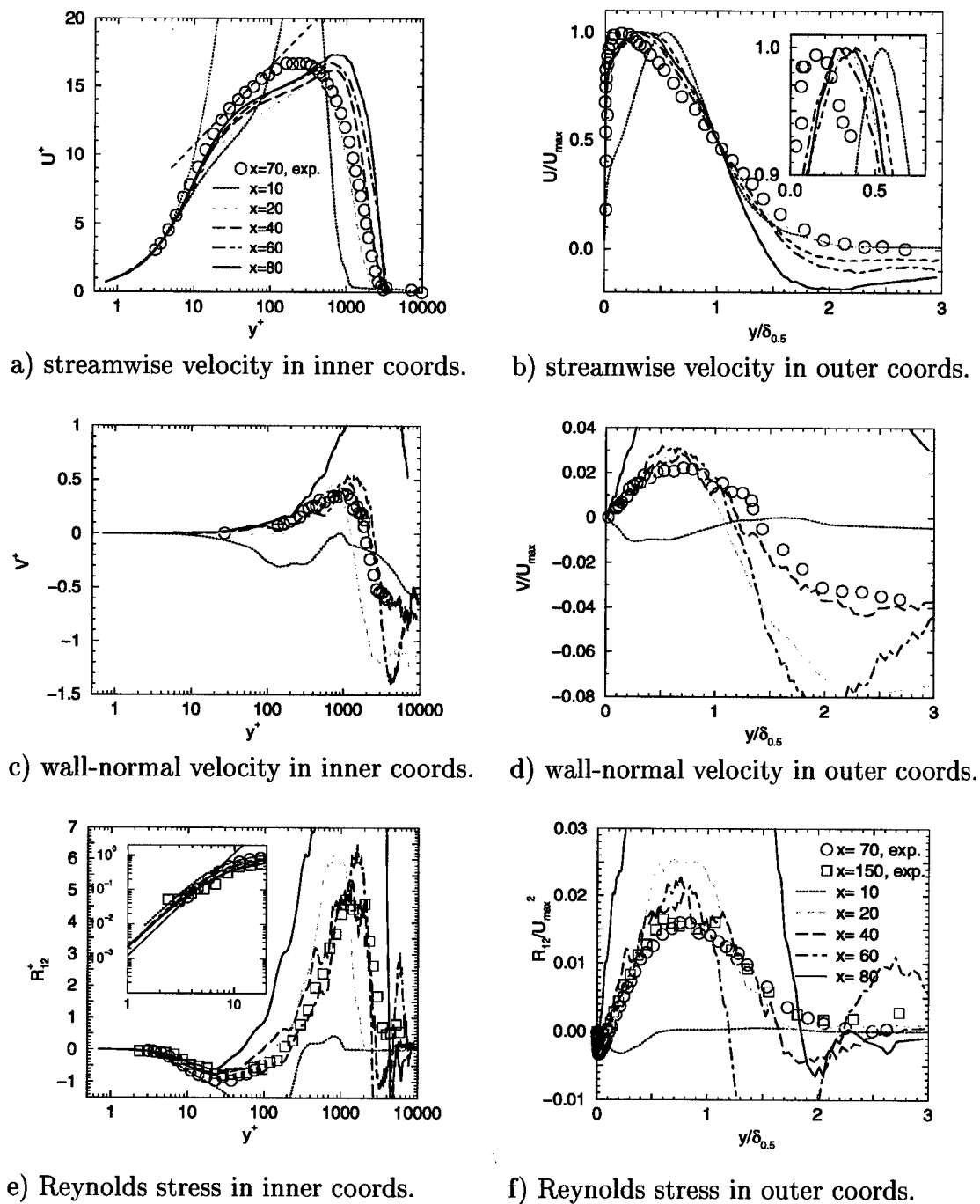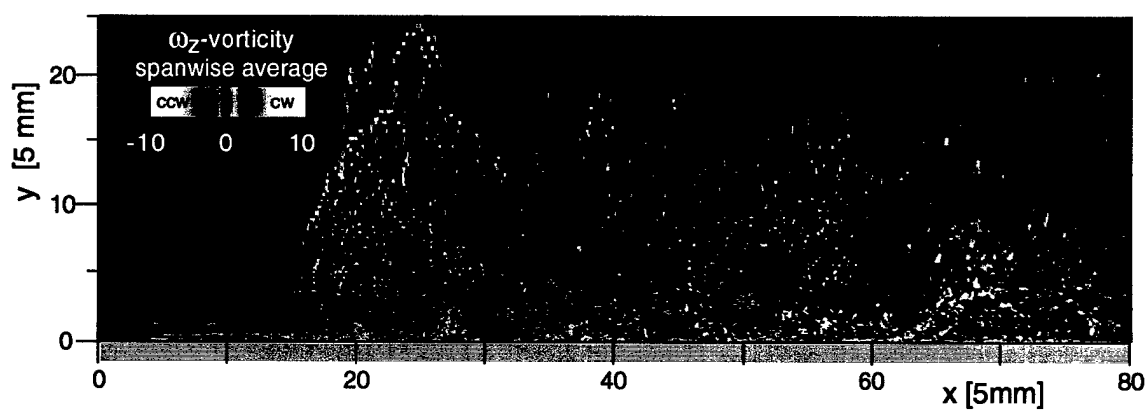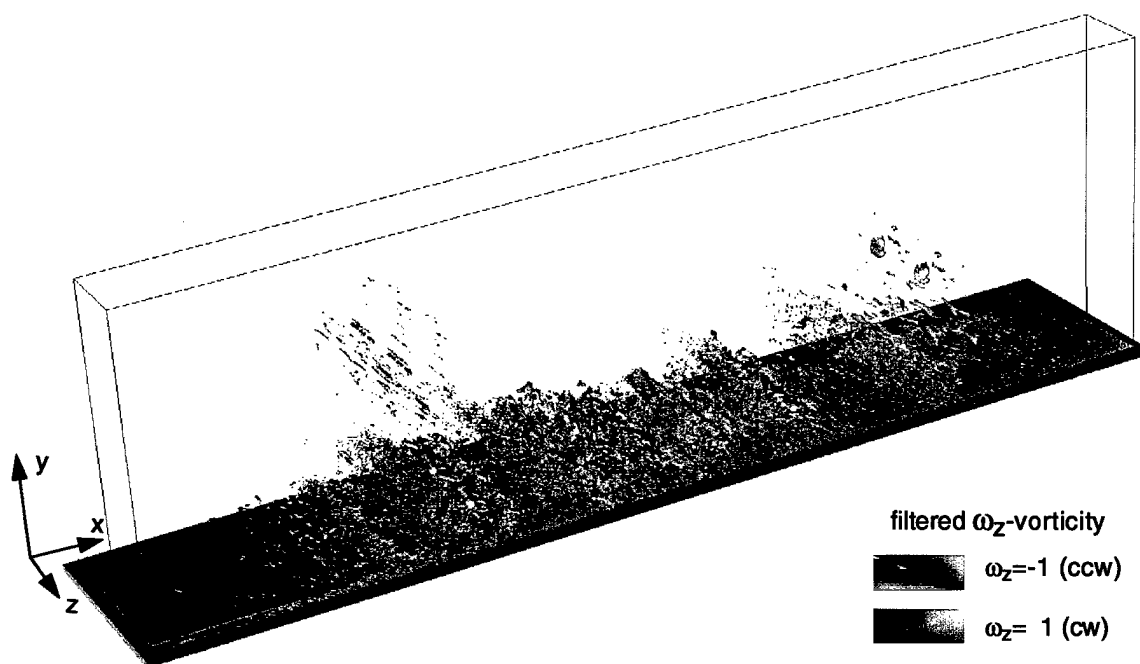
f) Reynolds stress in outer coords.

Figure 8: Time-averaged flow from a DNS of a turbulent plane wall jet. Shown are the streamwise and wall-normal velocities and the Reynolds stress in inner and outer coordinates at five streamwise locations. Also shown are measurements at $x = 70$ from experiments by Eriksson et al. (1998).
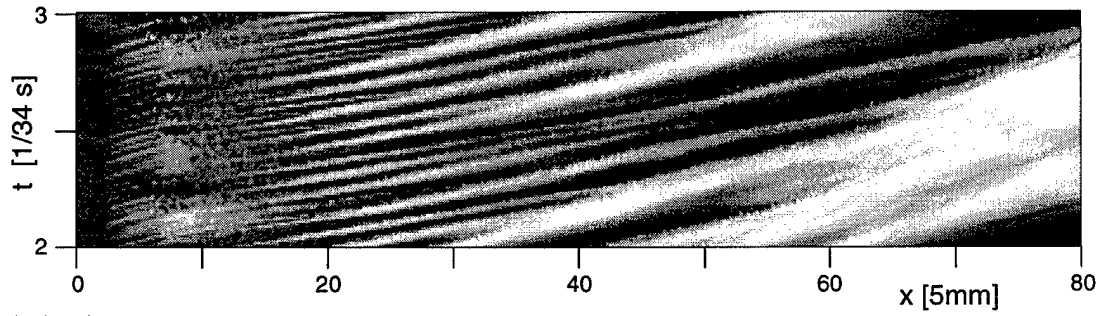
a) spanwise average



b) iso-surfaces

Figure 9: Snapshot from a DNS of a turbulent plane wall jet. Shown is the instantaneous spanwise vorticity at time t=2.5/34Hz.

An illustration of the wall vorticity in physical space is provided with the contour plots in Figure 10b shown at three time-instants versus streamwise and spanwise direction ($x-z$ plots). The spanwise direction is shown to scale over two wave length of $\lambda_z^{k=1} = 2$. Since the flow is computed with a symmetric DNS, the wall vorticity is periodic and symmetric in spanwise direction causing a regularity in the flow pattern in Figure 10b. Close to the forcing location, the flow is highly three-dimensional, but 2D structures begin to emerge at $x \approx 12.5$ and repeatedly double in size as they travel downstream.

The streamwise development of the 2D vortical disturbances can also be described with a Fourier decomposition in time of the spanwise averaged spanwise wall vorticity for each streamwise location. In the two contour plots in Figures 11, the Fourier amplitude of the wall vorticity and of the normalized wall vorticity are plotted as functions of frequency and streamwise location. In Figures 11a, the spectrum fills up rapidly downstream of $x \approx 12$. Over the interval between $x = 15$ and $x = 25$, high frequencies dominate, but farther downstream a clear shift in the spectrum towards lower frequencies occurs as seen in Figure 11b.

With our DNS we could demonstrate that 2D coherent structures develop in the turbulent plane wall jet and, as the jet spreads in downstream direction, adjust in size through vortex merging.
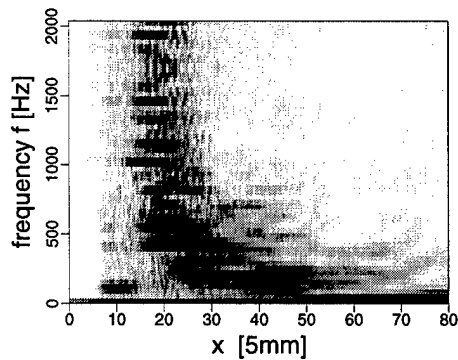
a) (x-t) diagram of the spanwise average
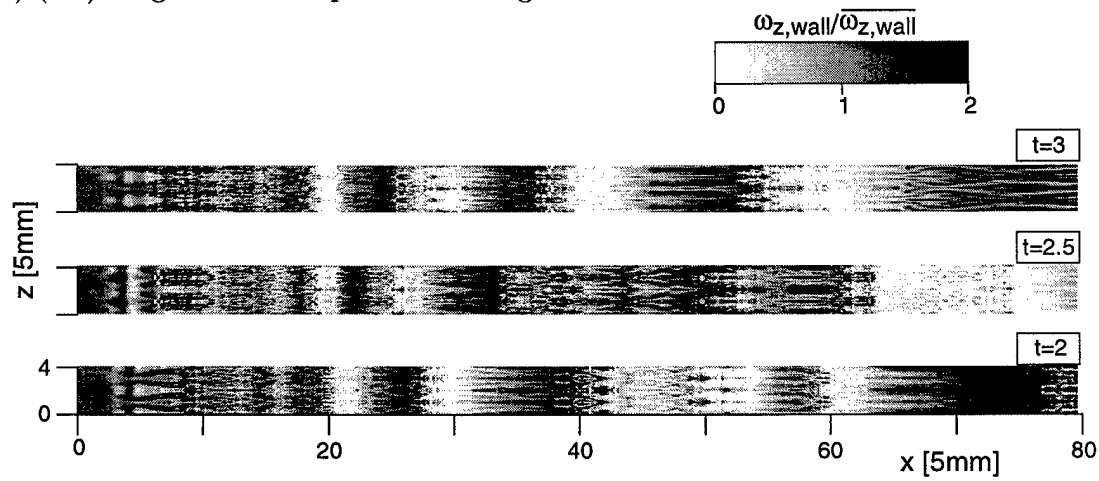


b) (x-z) plots at three time instants

Figure 10: Evolution of coherent flow structures in the turbulent plane wall jet generated through bypass transition. Shown is the spanwise wall vorticity.



a) spectrum not normalized      b) normalized with local time-average
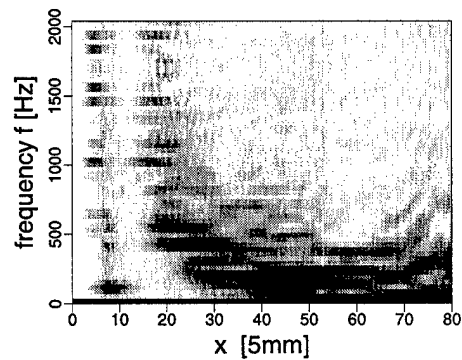
Figure 11: Fourier spectrum of the spanwise wall vorticity versus streamwise direction. Shown are grey-scales where black indicates the dominant frequencies in the spectrum.

## 4.2 DNS of Turbulent Wall Jet over Curved Surface

Encouraged by the success of the DNS calculations of the plane turbulent wall jet in section 4.1 we have performed DNS ofo the curved wall geometry (Coanda flow) with an otherwise identical computational setup with the same domain size, resolution, inflow conditions, and forcing method same as for plane wall jet. Only small steady volume forcing in the outer flow region was added to fix the location of any longitudinal vortices that might develop. The radius of the Coanda cylinder, $R = 0.8m$, in our DNS is several times larger than in the experiments by Wygnanski and Neuendorf (1999). This leads to a Görtler number[3] of $G\ddot{o} = 1300$ at the inflow. As a result of choosing a large-sized cylinder, the computational domain spans only about 30° of the cylinder circumference and does not contain the region of flow separation. The present computational setup was chosen due to numerical limitations of our current curved-wall Navier-Stokes code which requires a constant domain height and an equidistant grid in streamwise direction. Without the capability of adjusting the domain height to the rapidly spreading wall jet the computational cost of calculating the whole Coanda flow is too great. We have therefore focussed on the flow region upstream of the region of separation.

The Coanda flow computed in the curved wall DNS is very similar to the plane turbulent wall jet discussed in section 4.1. Snapshots of the flow field at one time-instant are provided in Figure 12, with color contours of the spanwise averaged spanwise vorticity shown in Figure 12a, iso-surfaces of the spanwise vorticity in Figure 12b. The 2D spanwise vortices in the outer flow region of the wall jet are clearly discernible, their dynamical behavior is comparable to that in the plane wall jet. Again the traveling vortices adjust in size to the spreading wall jet through vortex mergings.

However, due to curvature the Coanda flow is also Görtler-unstable in the outer flow region. As the wall jet spreads rapidly, the Görtler number does increase considerably as seen from the plot in Figure 13. Since the present calculation only allows

---

[3] The definition is given in equation (6).

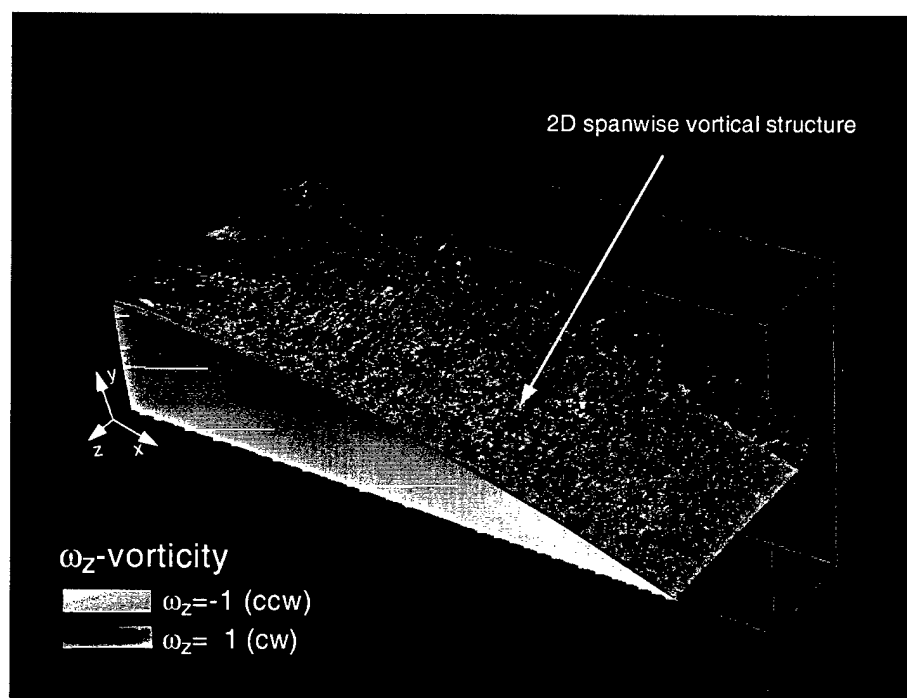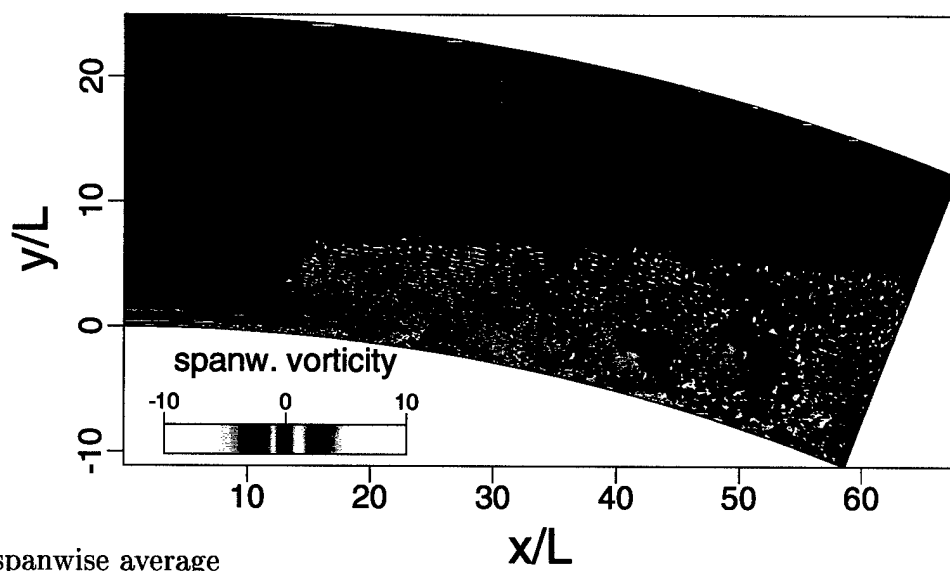a) spanwise average



b) iso-surfaces

Figure 12: Instantaneous flow field from the DNS of a turbulent wall jet over a curved surface. Shown are a) color contours of the spanwise average of the spanwise vorticity and b) iso-surfaces of spanwise vorticity.
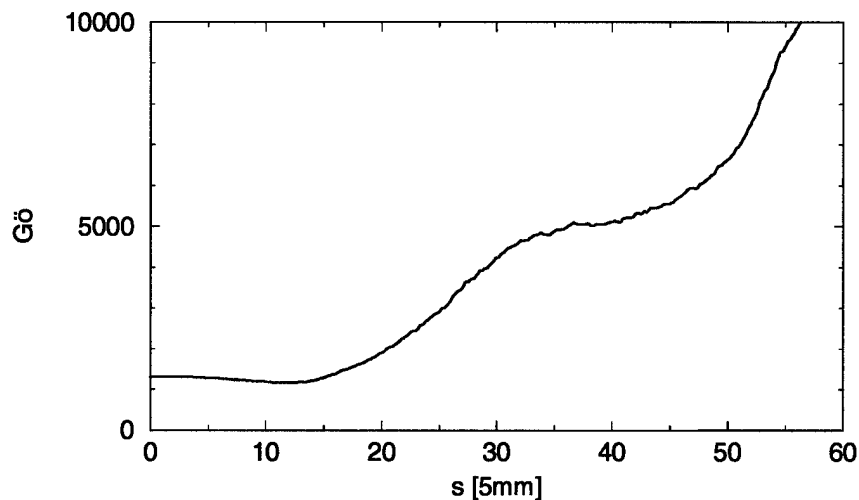
Figure 13: Streamwise development of the Görtler number for the simulated Coanda flow.

for symmetric Fourier modes in spanwise direction, a meandering of Görtler-type streamwise vortices as it occurs in the experiments by Neuendorf (2000) is inhibited. We therefore were able to isolate the streamwise vortices by simply time-averaging the streamwise vorticity. Shown in Figure 14 are the color contours of time-averaged streamwise vorticity at six streamwise locations. Also plotted for reference are streamwise mean flow profiles at these locations and the half width of the wall jet which indicates the spreading of the flow. Distinct vortices exist at $x = 10$ in direct response to the forcing, but they disappear almost completely during flow transition ($x = 20$). In the turbulent flow region, however, they reorganize and are clearly visible at $x = 30, 40$. Farther downstream, the computational domain is very narrow compared with the thickness of wall jet and the scale of the vortical structures which therefore cannot increase in width as they do in the experiment. To perform a more realistic calculation the domain width needs to be doubled or quadrupled, at twice or four times the computational cost. Alternatively, turbulence modeling can reduce resolution requirements and allow for efficient calculations with a wider computational domain.
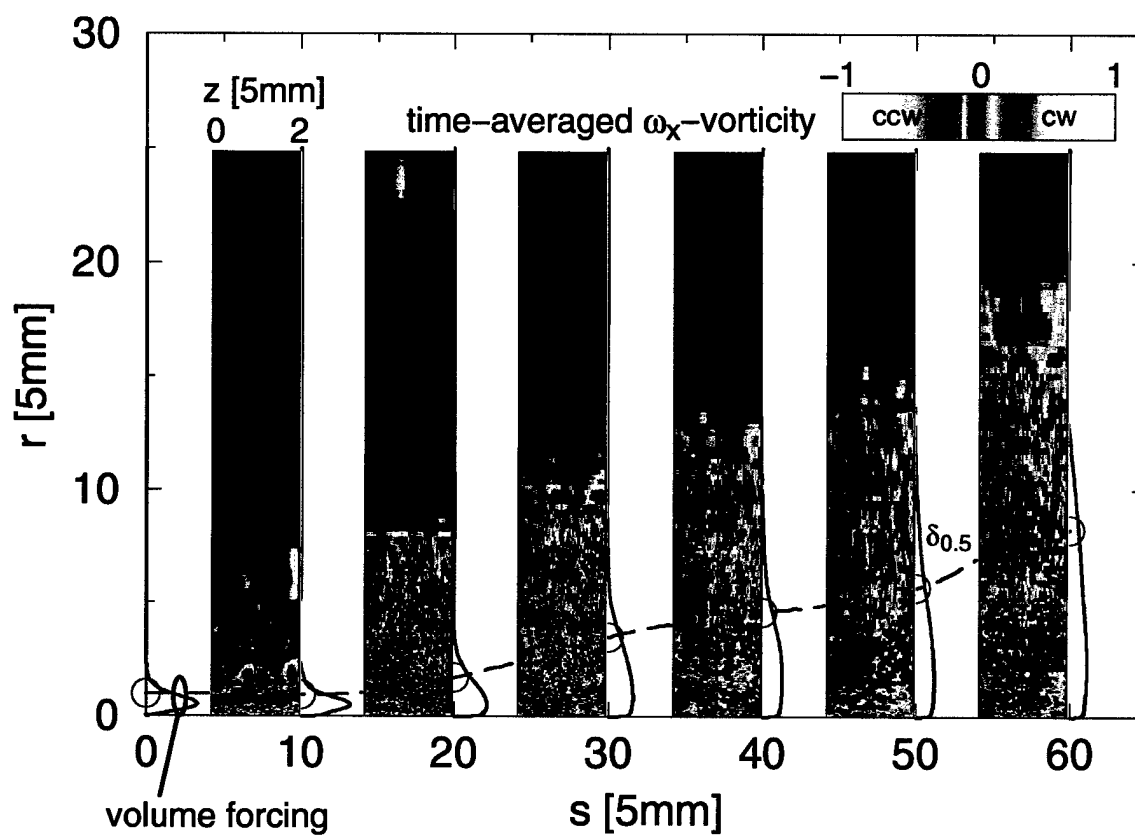
Figure 14: Development of streamwise vortices in the wall jet over a curved surface. Shown are color contours of time-averaged streamwise vorticity at six streamwise locations, the streamwise mean velocity profiles at these locations, and the half width of the wall jet.

## 4.3 FSM of Turbulent Wall Jet

When compared with DNS, turbulence modeling using the Flow Simulation Methodology can drastically reduce the computational effort for computing turbulent wall jets. A summary of the results from our FSM calculations will now be given.

The DNS from sections 4.1 and sec:BFcwj represent the fine grid limit of FSM for which the contribution function is zero. The other, the coarse grid limit is an Unsteady RANS where the contribution function is one. Many features of the turbulent wall jet can be captured with 2D URANS calculations. For example, in a turbulent wall jet a mismatch exists between the location of the maximum of the streamwise mean velocity profile and the zero stress location which is closer to the wall. Consequently, the Boussinesq approximation does not hold, and for modeling this effect using conventional, steady RANS complex non-equilibrium Reynolds stress models are required. As discussed in the paper by Wernz et al. (2002), the URANS calculations indicate that the mismatch between stress and strain results from a distortion of the mean flow due to the large coherent structures (computed in URANS) leading to a shift away from the wall of the maximum of the streamwise mean velocity profile and a shift towards the wall of the zero stress location.

URANS also provides an explanation for a a second phenomenon, the repeated vortex mergings observed in DNS of turbulent wall jets. Our URANS calculations of the forced turbulent wall jet suggest that subharmonic resonance occurs between a large amplitude primary disturbance and a small amplitude subharmonic disturbance. In the URANS calculation, the flow is forced with frequency $f = 34Hz$ at a large amplitude and also forcing with $f = 17Hz$ and $f = 8.5Hz$ at a much smaller amplitude. The forcing results in time-harmonic propagating disturbances as illustrated in the semi-logarithmic plot in Figure 15. Shown for the wall vorticity are the Fourier amplitudes of the fundamental and subharmonic disturbances versus x. The dashed curves represent the eigenbehavior of the disturbances which exhibit only moderate growth for all three forcing frequencies. In the presence of the large ampli-
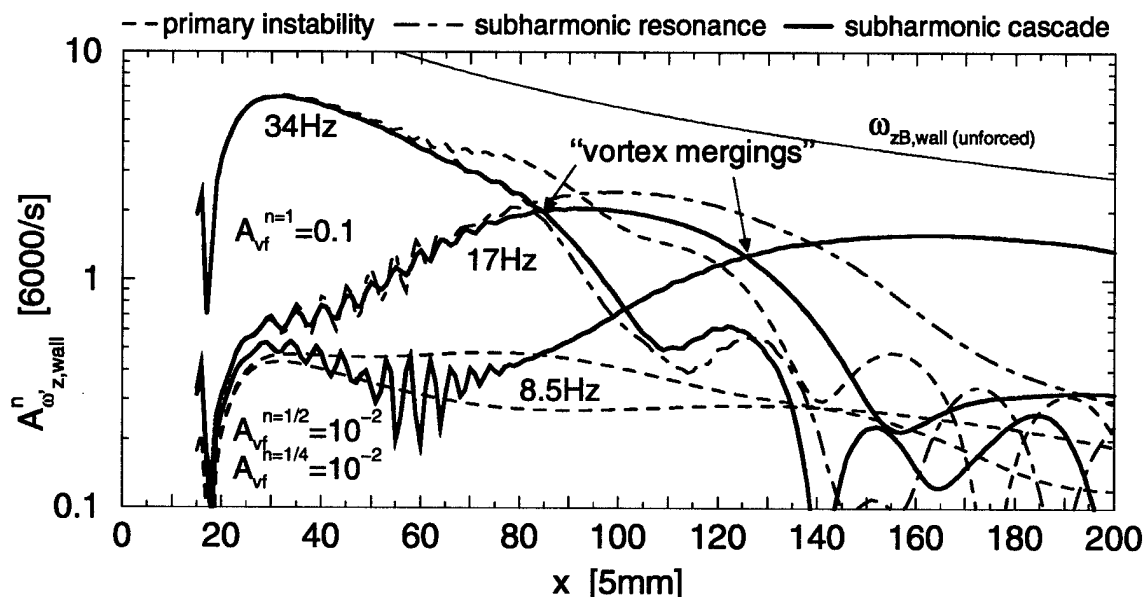
Figure 15: Subharmonic cascade in a forced turbulent wall jet ($Re_j = 10,000$) computed with URANS (Wernz 2001). Shown versus streamwise direction are the Fourier amplitudes of the time harmonics represented by wall vorticity.

tude primary disturbance with $f = 34Hz$ (solid blue line), however, the amplitude of the subharmonic disturbance (solid red line) grows rapidly, and surpasses that of the primary disturbance leading to the apparent vortex merging. This subharmonic, now the new large amplitude primary disturbance, in turn amplifies its own subharmonic (solid green line) leading to a second merging in this subharmonic resonance cascade.

One shortcoming of URANS is that the growth rates of primary disturbances is lower than in experiments. This is likely due to excessive damping of time-dependent structures by the turbulent stress from the turbulence model. In 3D FSM calculations where the value of the contribution function adjusts between zero and one depending on the local grid resolution, the turbulent stress term contributes less than in the URANS limit. In the FSM time-dependent structures, therefore, grow stronger and reach larger amplitudes than in the URANS calculations. This has been demonstrated with a case study for FSM presented in the paper by Wernz et al. (2002) a copy of

which is attached at the end of this report. In this case study, several FSM calculations with various grid resolutions and consequently different model contributions have been performed. These FSM calculations have the same computational setup as the DNS in section 4.1 with the same 3D forcing employed to trigger flow transition. The turbulence model is adjusted once breakdown has occurred. Snapshots of the flow field from five FSM cases are presented in Figure 16, a DNS (case F1), an LES-like FSM (case F2), an FSM with a coarse (case F3) and an even coarser resolution (case F4) and a URANS calculation (case F5). Shown are color contours of spanwise vorticity, to the left the spanwise averaged vorticity and to the right the wall vorticity. As the model contribution increases from case F1 (0%) to case F5 (100%), the small scale structures disappear but, except for the URANS in case F5, the large scale structures are preserved.

To show the effect of the turbulence model on the mean flow, in Figure 17 the streamwise mean velocity computed with the various FSM cases are compared with the experimental measurements by Eriksson et al. (1998). Shown for cases F1-F5 are the streamwise velocity profiles in inner coordinates at one streamwise location. The observed trends are extremely encouraging. The velocity profiles for FSM cases F2-F4 are closer to the experimental data that the profile from URANS, case F5. In particular, cases F2-F4 exhibit the "log-like" layer which is measured experimentally and is not captured by conventional RANS calculations. Case F2, the LES-like FSM which has the same grid resolution as the DNS (case F1), appears closest to the measurement data.

a) Case F1 (DNS)



b) Case F2 ("LES")



c) Case F3 ("coarse LES")



d) Case F4 ("coarse LES")



e) Case F5 (URANS)

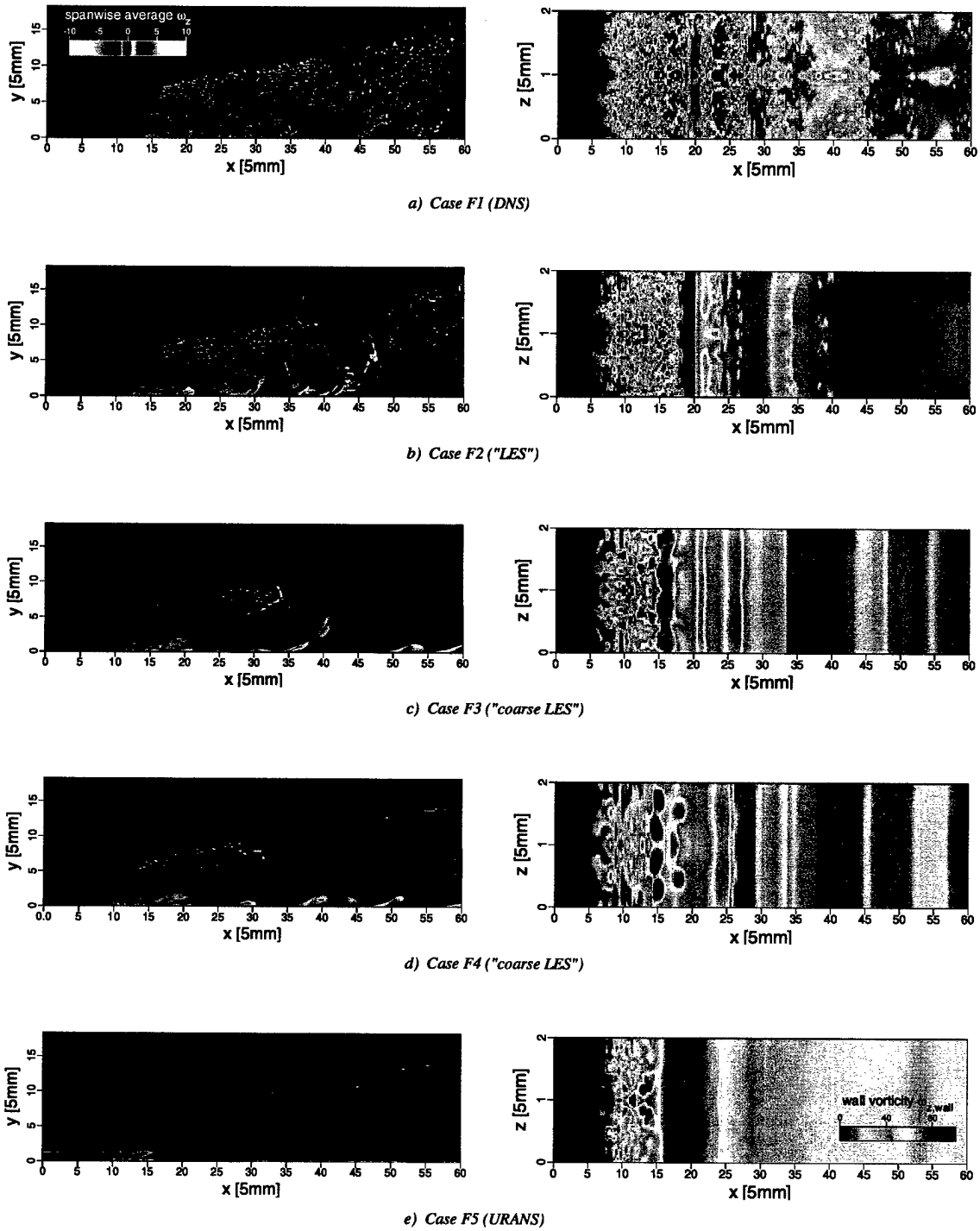Figure 16: Instantaneous flow fields from the FSM calculations (Cases F1-F5) at time $t = 2/34Hz$. Shown are color-contours of the spanwise average of the spanwise vorticity (left) and the spanwise vorticity at the wall (right).
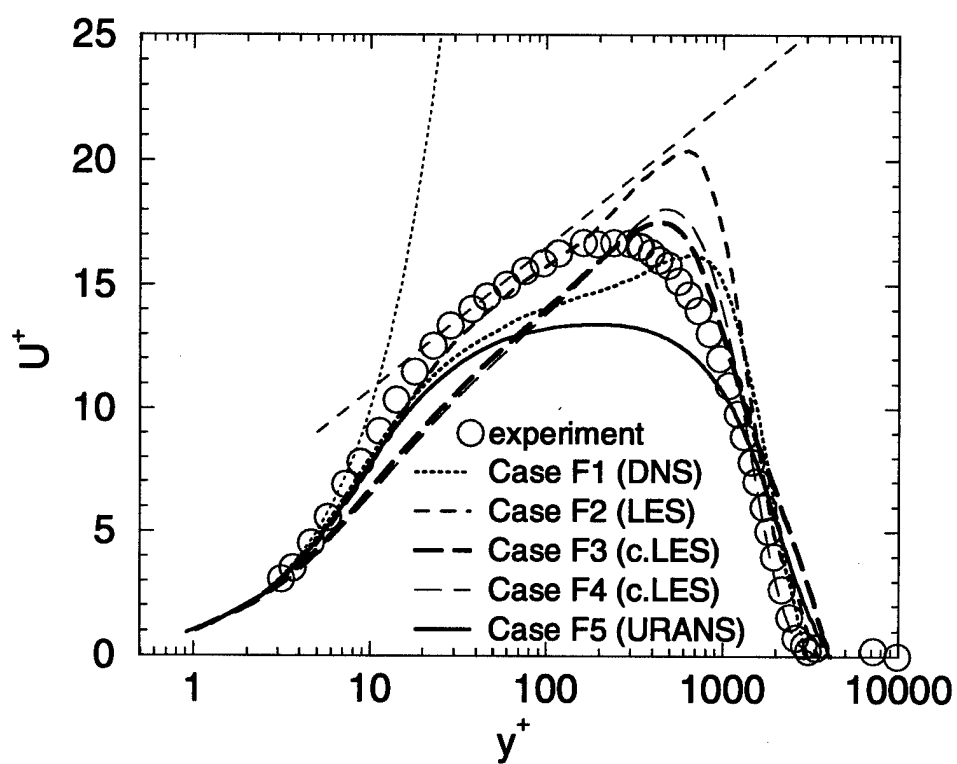
Figure 17: Mean streamwise velocity profiles from FSM calculations (Cases F1-F5) in inner coordinates. Also shown are measurements from experiments by Eriksson et al. (1998).

# 5 Results from Calculations with the Immersed Boundary Technique

With the Cartesian grid method using immersed boundary techniques, the entire Coanda flow can be computed in one calculation including the nozzle geometry and the region of flow separation. This enables, for example, investigations of the effect of the nozzle geometry on the global flow field. Traditionally, immersed boundary techniques have been used in conjunction with computational methods of low order accuracy (up to second order). Therefore, a strong effort is being made in our research group to determine the impact of using IBT in conjunction with our higher order methods and to further develop IBT so that overall numerical accuracy is preserved. Some benchmark calculations are now presented followed by a discussion of our results for the Coanda flow.

## 5.1 Validation Cases

Our Cartesian grid approach has been validated with three key benchmark cases which address different performance features of the method: the backward-facing step, Tollmien-Schlichting waves in a flat-plate boundary layer, and the cylinder in a free stream at low Reynolds number. Detailed results from the first two test cases have been reported in the paper by Terzi et al. (2001).

The Backward-facing step is a standard benchmark case for CFD codes where the reattachment length may be influenced by numerical inaccuracies, e.g. excessive numerical viscosity. The flow physics is primarily driven by the shear layer that develops from the step corner and near-wall accuracy at the boundary is not crucial for obtaining sufficiently good results. We have compared various IBT calculations using different boundary treatments with the flow solution from a previously validated body-fitted grid calculation. Results from two of these calculations, one using the feedback control method by Goldstein et al. (1993) the other the direct method by Mohd-Yusof (1997) are illustrated in Figure 18. In both cases (Figure 18b&c),
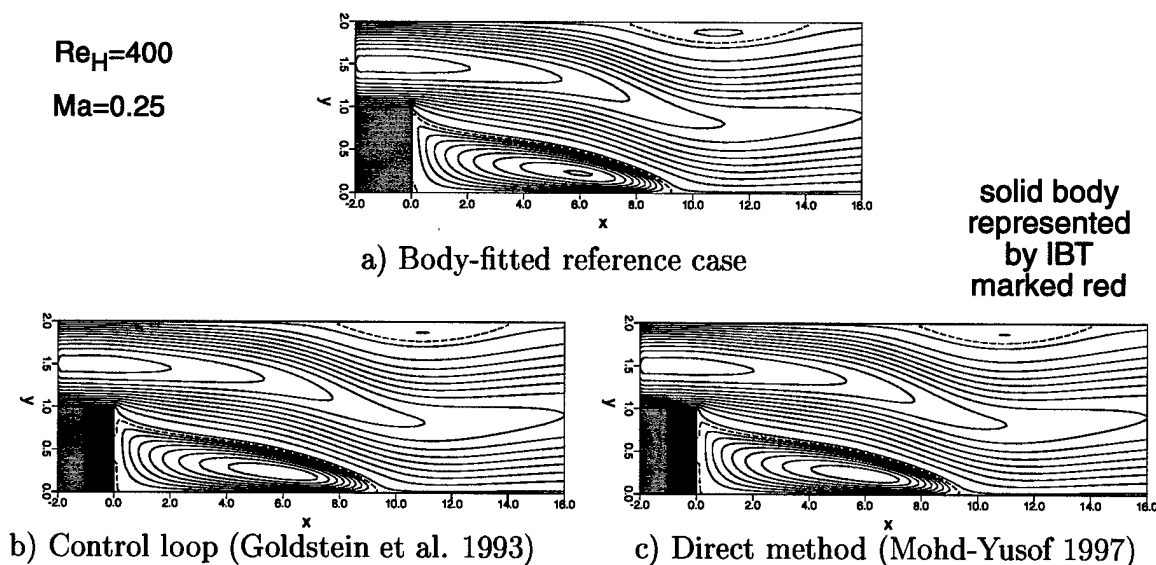
Re_H=400

Ma=0.25

solid body
represented
by IBT
marked red

a) Body-fitted reference case

b) Control loop (Goldstein et al. 1993)     c) Direct method (Mohd-Yusof 1997)

Figure 18: Backward-facing step flow; u-velocity contours for body-fitted grid computation and for two IBT methods, immersed boundary techniques applied to the red area only.

the IBT is applied over an area adjacent to the step base marked red. Plotted are contour lines of streamwise velocity, $u$, with a dashed line for $u = 0$ which marks the separation point at the wall. Clearly, both IBT results are in excellent agreement with the body-fitted reference case in Figure 18a. In particular, their reattachment points match up very well.

In contrast to the backward-facing step flow, near-wall accuracy is crucial for correctly predicting the growth of Tollmien-Schlichting (T-S) waves. Results from the calculations by Terzi et al. (2001) are presented in Figure 19 with an illustration of the computational setup in Figure 19a. In these calculations, various IBT methods with and without wall corrections are compared with linear stability theory and a DNS on a body-fitted grid. While the wall-normal amplitude distribution of the streamwise velocity component agrees well for all cases (Figure 19b), the phase difference between the streamwise and wall-normal disturbance velocity components close to the immersed boundary varies strongly for different methods (Figure 19c).

a) computational setup

LST– linear stability theory
B – body–fitted
D – direct method
G – control–loop method
I – incompressible code
S – solid–body correction
R – reflection correction
C – one–sided correction

b) u-disturbance amplitude distribution

c) phase difference between u & v dist.

d) amplitude for second order methods

e) amplitude for fourth order methods
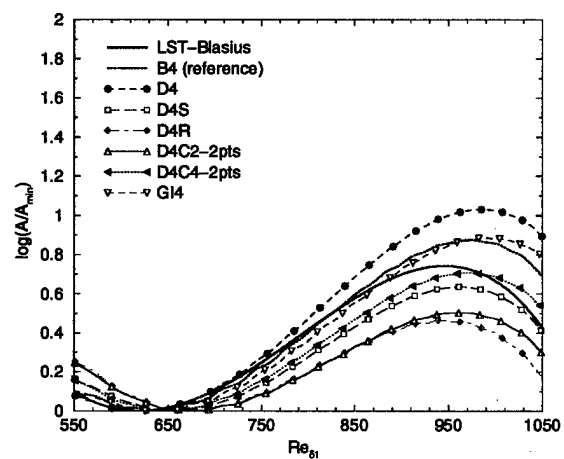
Figure 19: Tollmien-Schlichting wave simulation: comparison of results from various IBT methods with linear stability theory and results from DNS with body-fitted grid.

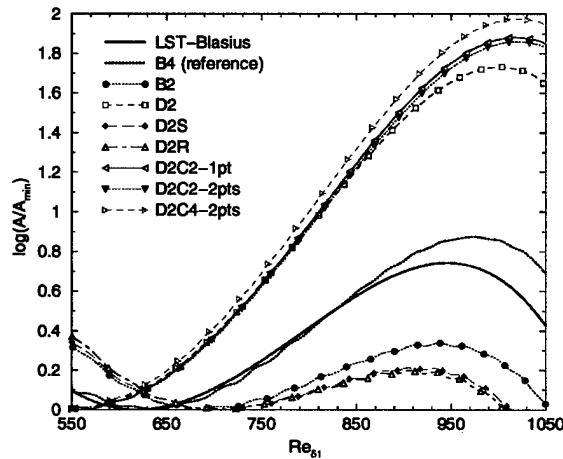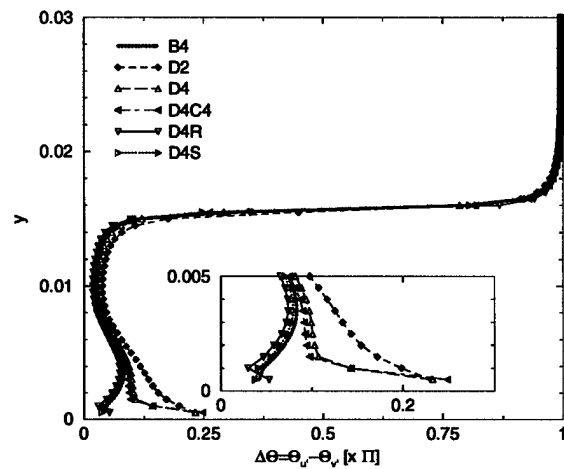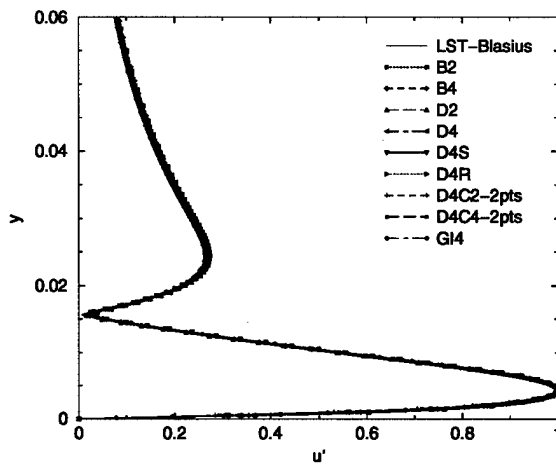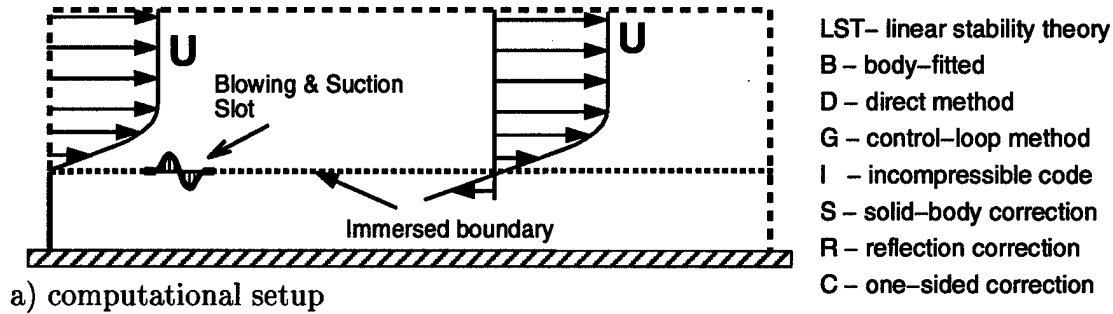Since this phase difference has a strong influence on the downstream growth of the TS-wave, a significant spread results in the growth prediction from the different methods (Figure 19d&e), particularly for second order methods. For higher grid resolution (with significantly increased computational cost), the agreement of IBT with the DNS using a body-fitted grid does improve, however. The conclusion is that for computing the development of time-dependent disturbances that are driven by wall instabilities, current IBT methods are less accurate than higher-order body-fitted grid method (used for the calculations in section 4) and need further improvement.

In the two previous tests the immersed boundaries are aligned with the grid, which is not the case for the Coanda cylinder. We have therefore tested the IBT for a third standard benchmark case, the cylinder in a uniform freestream, which is close to the Coanda flow geometry. Using either IBT variants considered, the direct method and the feedback control method, a Karman vortex street is obtained (Figure 20). The Strouhal number for the vortex shedding is $St = 0.23$ for the direct method and
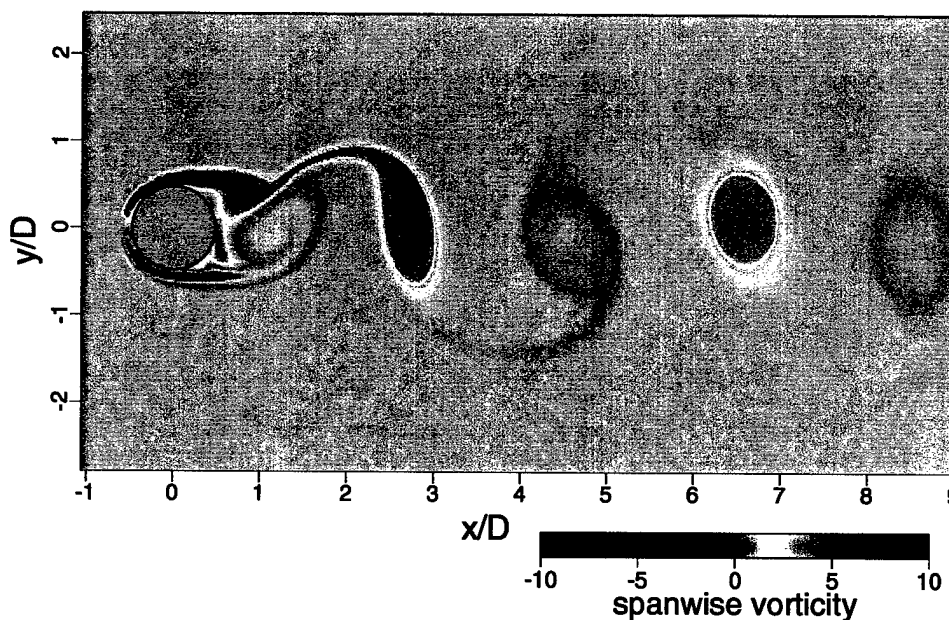


Figure 20: Flow around cylinder in a uniform freestream computed using IBT ($Re_D = 400, Ma = 0.2$). Shown are color contours of spanwise vorticity where the cylinder is indicated by the grey shaded area.

$St = 0.22$ for the feedback control method which is in excellent agreement with the literature (e.g. $St = 0.22$ reported by Saiki and Biringen 1996). This leads to the conclusion that the IBT appears capable of computing separated flows over curved surfaces and is suited for computing the Coanda flow.

## 5.2 DNS of Coanda Flows

The IBT approach has enabled us to compute the whole Coanda flow field including the mass supply inside the cylinder. In our calculations, the experimental setup from experiments by Wygnanski and coworkers was modeled including the plenum chamber inside the cylinder. At this point, 2D DNS of the laminar Coanda flow have been performed. In the present simulations, the Coanda flow is generated by applying a mass source inside the plenum chamber of the cylinder. Results from one such IBT calculation are plotted in Figure 21. Shown in Figure 21a are color contours of spanwise vorticity. The jet exits the nozzle at $\theta_0 = 270°$ and remains attached up to $\theta_{sep} \approx 150°$. As shown with the perspective view of the pressure distribution in Figure 21b, the mass source causes a pressure build up inside the cylinder, where the pressure, $p_0$, is about 20% above ambient pressure, $p_\infty$. Over the nozzle contraction, the pressure drops as the fluid accellerates and the surface pressure, $p_s$, is below $p_\infty$ throughout the length of the attached flow region. The Mach number (Figure 21c) peaks at $Ma = 0.4$ at the nozzle exit but then drops rapidly below 0.3, so the flow remains mostly incompressible. Due to the flow acceleration, the temperature inside the cylinder (Figure 21d) drops a few percent below ambient temperature. This small variation may be further reduced by adding the mass at a temperature slightly above ambient.

In a parameter study, the effect of the nominal Reynolds number on the length of the attached flow region of the Coanda flow has been investigated. The goal has been to keep the wall jet attached for as long as possible. Flow parameters for the cases
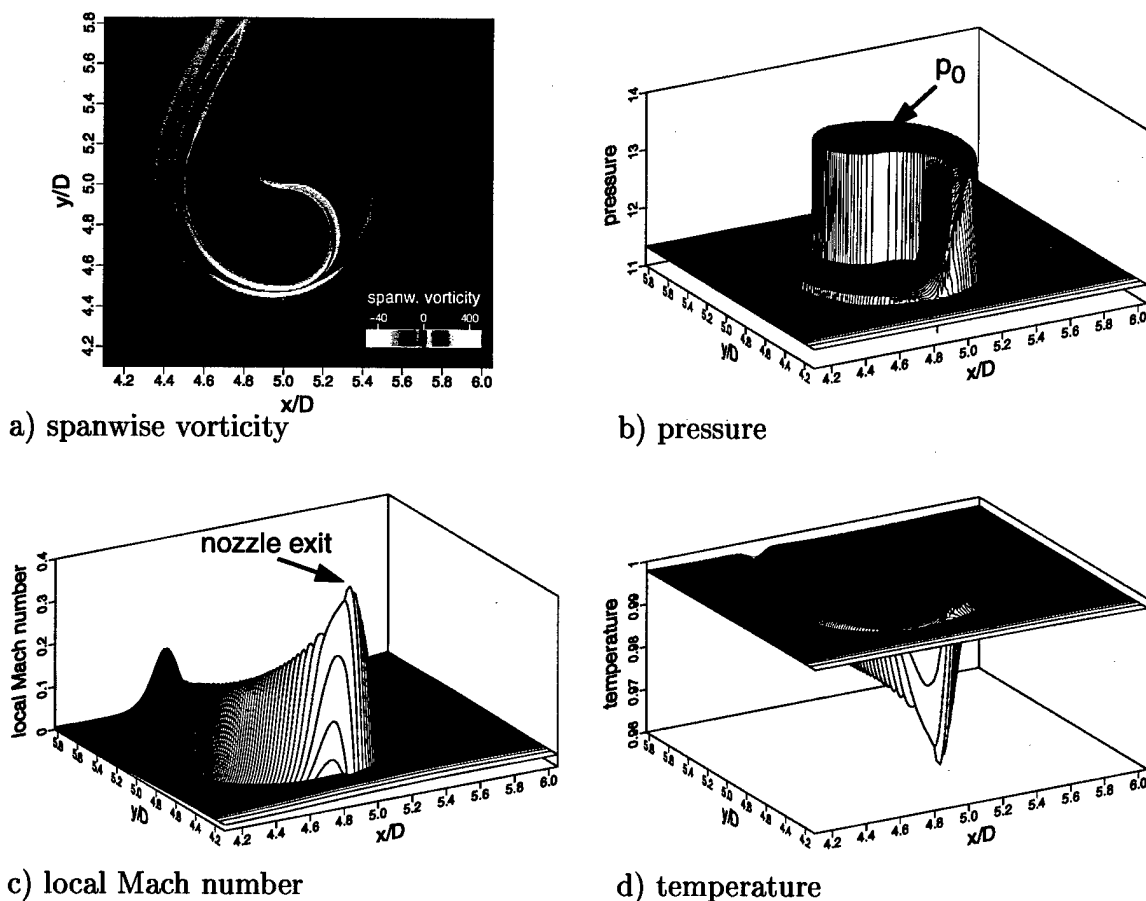
a) spanwise vorticity



b) pressure



c) local Mach number



d) temperature

Figure 21: Laminar Coanda flow computed using IBT. Shown is the stationary flow field from case 3 (see Table 1).

are listed in Table 1.[4] For case 1 (Figure 22a) which has the lowest Reynolds number, $Re_N = 75$, the flow spreads rapidly after exiting the nozzle and separates after a short distance of about 60° from the nozzle. In this case, the jet is not energetic enough to remain attached for very long. In cases 2-5 (Figure 22b-e), as the Reynolds number is further and further increased, the separation location moves farther and farther downstream. From our experience, and not surprisingly, a thin jet with high jet exit momentum works best in keeping attached. In fact, in inviscid flow calculations, where $Re_N \rightarrow \infty$, the flow adheres to the cylinder all the way around, for 360°.

[4] A definition for pressure coefficient, $c_p$, and nominal Reynolds number, $Re_N$, is given in equations (2) and (3) respectively.

| case | 1 | 2 | 3 | 4 | 5 | 6 (suction) | 7 |
|---|---|---|---|---|---|---|---|
| nozzle width/radius, $b/R$ | 0.1 | 0.1 | 0.1 | 0.05 | 0.05 | 0.05 | 0.1 |
| nozzle angle, $\theta_0$ | 135° | 270° | 270° | 270° | 270° | 270° | 270° |
| nominal Reynolds number, $Re_N$ | 75 | 250 | 450 | 740 | 610 | 610 | 640 |
| pressure coeff., $c_p(\theta - \theta_0 = 80°)$ | 0.01 | 0.07 | 0.4 | 0.27 | 0.19 | 0.13 | — |
| separation angle, $\theta_{sep} - \theta_0$ | 60° | 88° | 122° | 140° | 130° | 143° | — |

Table 1: Parameters for laminar Coanda flow calculations using IBT.

For the viscous flow computed with a time-accurate scheme, however, the Coanda flow becomes more and more unstable to two-dimensional vortical disturbances. It becomes increasingly difficult to reach a stationary state. In order to stabilize the flow, as a remedy, wall suction has been applied near the nozzle exit in case 6 (Figure 22f) which other than that is identical to case 5 (Figure 22e) without wall suction. As a result, the amplitude of the vortical disturbances is drastically reduced and the flow remains attached farther than in case 5. How destructive the two-dimensional vortical structures can by for the laminar Coanda flow is illustrated for case 7 ($Re_N = 740$) in Figure 23, where two-dimensional counter-rotating vortex pairs repeatedly disrupt the flow during startup and propel themselves through mutual induction away from the wall. This process has also been observed for laminar plane wall jets (Wernz and Fasel 1996). In three-dimensional calculations, however, this 2D mechanism is in competition with 3D instabilities in the flow that strongly reduce the strength of the near-wall vortex and thus mostly prevent the ejection process from occurring (Wernz and Fasel 1999).

a) Case 1: $Re_N = 75$

b) Case 2: $Re_N = 250$

c) Case 3: $Re_N = 450$

d) Case 4: $Re_N = 740$

e) Case 5: $Re_N = 610$

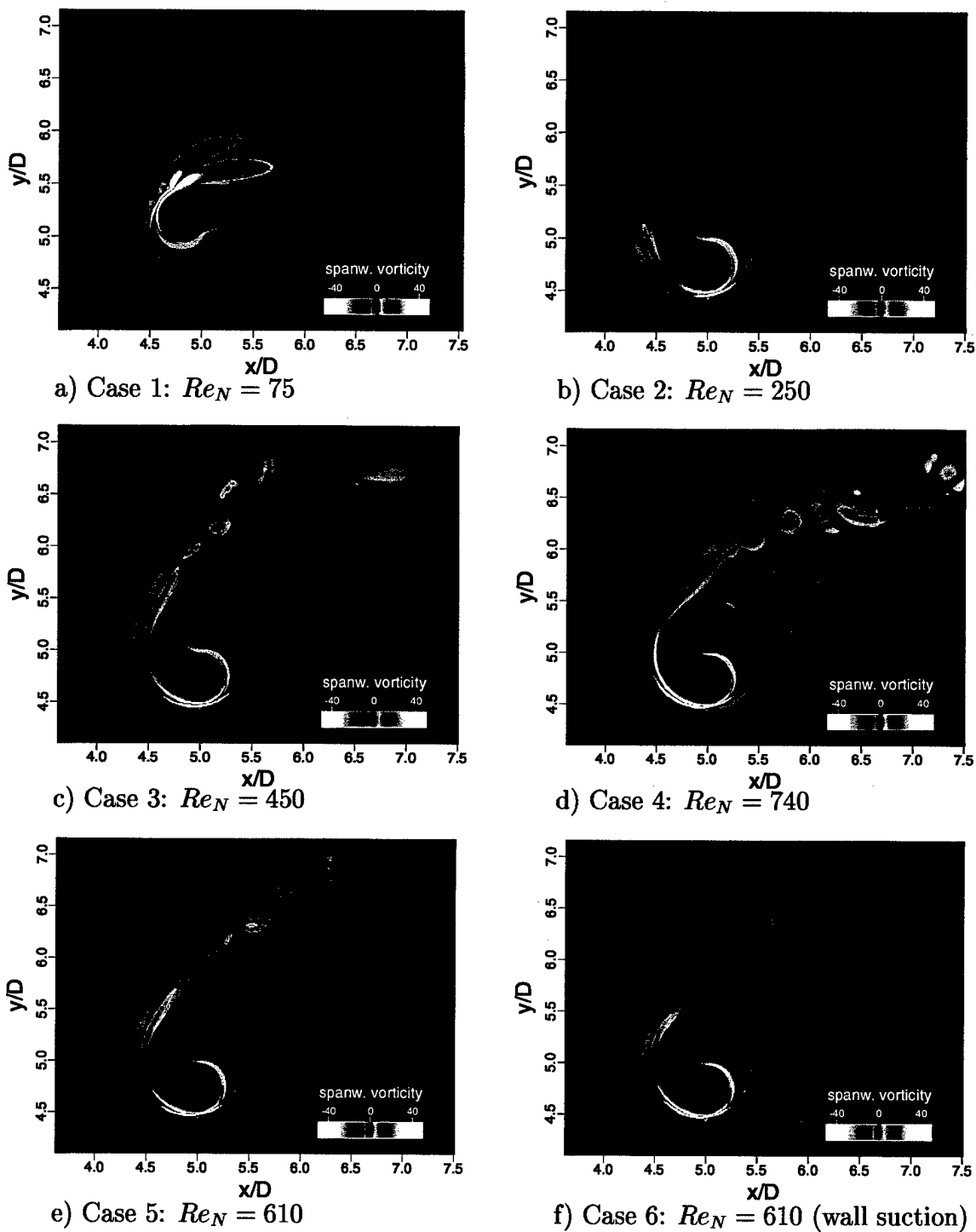f) Case 6: $Re_N = 610$ (wall suction)

Figure 22: Parameter study on the effect of the nominal Reynolds number $Re_N$ on the Coanda flow. Shown are color contours of spanwise vorticity.
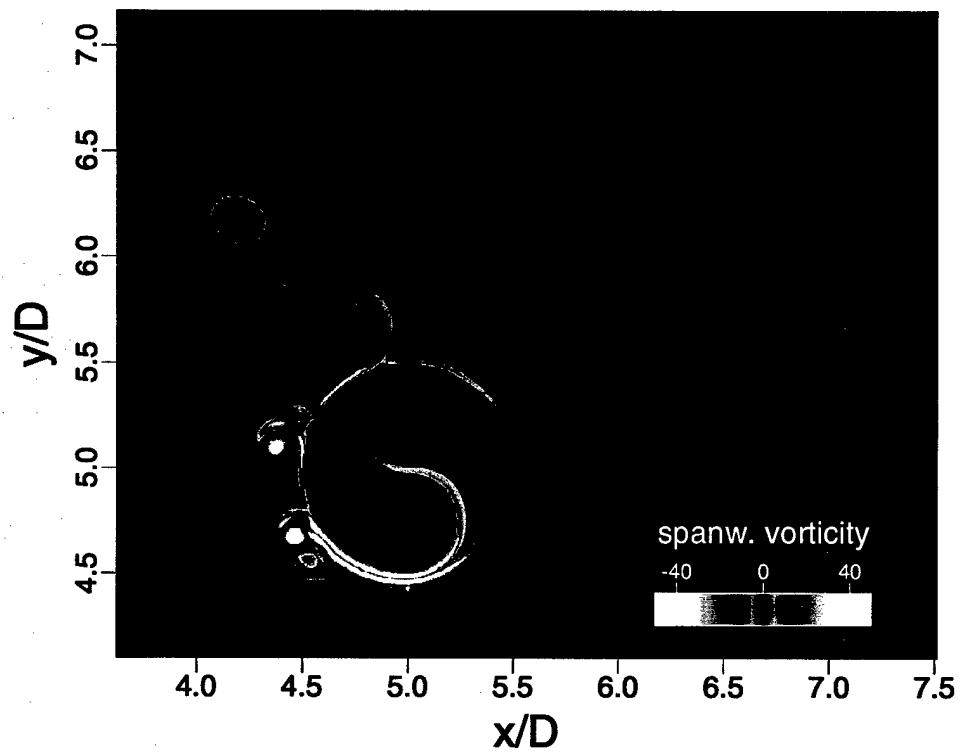
Figure 23: Snapshot of the flow field from case 7 (see Table 1) where no stationary state was reached. Shown are color contours of spanwise vorticity.

# 6  Summary and Outlook

In the present research project we have investigated turbulent wall jets on Coanda cylinders as prototypes for separating flows over curved-wall geometries. Two computational approaches have been taken, both providing valuable insight for further research.

The flow over a segment of the Coanda cylinder has been investigated using Direct Numerical Simulations (DNS) on a body-fitted grid. With DNS, the development of large 2D coherent structures in both, plane and curved wall jets, has been investigated. These 2D vortical structures emerge in the outer flow region of the wall jet during flow transition and persist far into the turbulent flow regime. They adjust in size to the spreading wall jet through repeated vortex mergings. Using URANS calculations, evidence was found that subharmonic resonance may be the mechanism that leads to these vortex mergings. For the curved wall jet, longitudinal vortical structures have been found in the outer region of the wall jet. These Görtler-type vortices also grow in size as the wall jet spreads. Due to the narrow computational in the present DNS, however, a spread in spanwise direction is inhibited, which possibly leads to unnaturally narrow vortices. The Flow Simulation Methodology (FSM) has been adapted for wall jet calculations as a new approach for computing this non-equilibrium flow more cost-effectively. In FSM calculations of the plane wall jet, it was demonstrated that the correct mean flow and development of the large structures can be computed with coarsely resolved FSM that are an order of magnitude less costly than DNS. As the next future step, the FSM now will be applied to curved wall jets to allow for wider domains in spanwise direction than in the present DNS. This will allow the longitudinal vortices to adjust in size in downstream direction. A realistic simulation of the flow containing both, streamwise and spanwise structures will enable us to study their interaction and actively influence their role in the flow separation process of the Coanda wall jet farther downstream. Also, two current computational limitations of our Navier-Stokes code using a body-fitted grid, the constant domain

height and equidistant grid in streamwise direction, must be overcome to employ this approach for computing the actual flow separation process.

We have also initiated a second, novel computational approach, a Cartesian grid method using the immersed boundary technique which enables us to compute the entire Coanda flow including nozzle and separated flow region. In our preliminary calculations of 2D laminar flows around a Coanda cylinder, we were able to keep the flow attached up to about 140° from the nozzle, Major trends could be captured, namely that greater jet momentum and thinner jets lead to delayed separation, that larger jet momentum favors the development of 2D coherent structures, which in turn promote early separation. Since near-wall effects may have an impact on the flow separation process further efforts will be made to improve the accuracy of the gradients at the immersed boundaries. Also, our calculations are presently limited to 2D laminar flow due to computational cost. For efficiently applying the Cartesian grid method to predict flows at higher Reynolds numbers and turbulent flows, a localized gridmesh refinement is required near the body surface and other flow regions with large gradients, e.g. the Adaptive Mesh Refinement approach (AMR). Such a grid refinement capability is currently being implemented into the code.

# 7 References

Eriksson, J.G., Karlsson, R., I., and Persson, J., 1998. "An Experimental Study of a Two-Dimensional Plane Turbulent Wall Jet." *Exp. in Fluids* **25**, 50-60.

Gatski, T. and Speziale, C., 1993. "On Explicit Algebraic Stress Models for Complex Turbulent Flows." *J. Fluid Mech.* **254**, 59-78.

Goldstein, D., Handler, R., and Sirovich, L., 1993. "Modeling a No-slip Flow Boundary with an External Force Field." *J. Comp. Phys.*, 105:354–366, 1993.

Harris, P.J., 1997. "Numerical Investigation of Transitional Compressible Plane Wakes." Ph.D. Thesis, The University of Arizona, 1997.

Kloker, M., Konzelmann, U., and Fasel, H., 1993. "Outflow Boundary Conditions for Spatial Navier-Stokes Simulations of Transitional Boundary Layers." *AIAA J.* **31 (4)**.

Meitz, H.L. and Fasel, H.F., 2000. "A Compact-Difference Scheme for the Navier-Stokes Equations in Vorticity-Velocity Formulation." *J. Comp. Phys.*, **157**, 3721-403.

Mohd-Yusof, J., 1997. "Combined Immersed-Boundary/B-Spline Methods for Simulations of Flow in Complex Geometries." *Center for Turbulence Research Briefs*, 317-327.

Neuendorf, R. and Wygnanski, I., 1999. "On a Turbulent Wall Jet Flowing Over a Circular Cylinder." *J. Fluid Mech.* **381**, 1-25.

Neuendorf, 2000. "Turbulent Wall Jet Along a Convex Curved Surface." Dissertation, Technische Universität Berlin.

Newman, B.G., 1961. "The Deflection of Plane Wall Jets by Adjacent Boundaries – Coanda effect." In *Boundary Layer and Flow Control*. G.V.Lachman (ed.), Pergamon Press, 232-251.

Seifert, A., Bachar, T., Koss, D., Shepshelovich, M., and Wygnanski, I., 1993. "Oscillatory Blowing: A Tool to Delay Boundary-Layer Separation." *AIAA J.* **31**, 2052-2059.

Seifert, A., Darabi, A., Sokolov M., and Wygnanski, I., 1994. "The Use of Oscillatory Blowing for Managing the Flow Around a Slotted Airfoil at Low Reynolds Numbers." Euromech Colloquium 328, Management and Active Control of Turbulent Shear Flows, Technische Universität Berlin.

Saiki, E.M. and Biringen, S., 1996. "Numerical Simulation of a Cylinder in Uniform Flow: Application of a Virtual Boundary Method." *J. Comp. Phys.*, 123:450–465.

Speziale, C., 1998. "Turbulence Modeling for Time-Dependent RANS and VLES: A Review." *AIAA J.* **36**, 173-184.

Tannehill, J.C. , Anderson, D.A. , and Pletcher, R.H., 1997. "Computational Fluid Mechanics and Heat Transfer." McGraw-Hill, 2nd edition.

von Terzi, D.A., 1998. "Towards Controlling the Flow Behind a Backward-Facing Step." Master's Thesis, The University of Arizona.

von Terzi, D. A., Linnick, M. N., Seidel, J., and Fasel, H. F., 2001. "Immersed Boundary Techniques for High-Order Finite-Difference Methods." AIAA Paper 01-2918.

Wernz, S. and Fasel, H., 1999. "Numerical Investigation of Resonance Phenomena in Wall Jet Transition." In *Laminar-Turbulent Transition* (ed. H. F. Fasel & W. S. Saric), pp. 217–222. Springer Verlag, IUTAM Symposium, Sedona, Az.

Wernz, S. and Fasel, H.F., 1996. "Numerical Investigation of Unsteady Phenomena in Wall Jets." AIAA Paper 96-0079.

Wernz, S., 2001. "Numerical Investigation of Forced Transitional and Turbulent Wall Jets." Ph.D. Dissertation, The University of Arizona.

Wernz, S., Seidel, J., and Fasel, H., 2002. "Numerical Investigation of Turbulent Wall Jets." 40th AIAA Aerospace Sciences Meeting & Exhibit, Reno, NV, January 14-17.

Wygnanski, I., 1997. " Boundary Layer and Flow Control by Periodic Addition of Momentum (invited)." AIAA Paper 97-2117.

Zhang, H.-L. and Fasel, H., 1999. "Direct Numerical Simulation of the Turbulent Flow over a Stratford Ramp." AIAA Paper 99-3359.

# 8   Publications and Presentations at Conferences

Wernz, S., 2001. "Numerical Investigation of Forced Transitional and Turbulent Wall Jets." Dissertation, The University of Arizona.

Wernz, S. and Fasel, H., 2001. "Numerical Investigation of Resonance Mechanisms in Transitional and Turbulent Wall Jets Using DNS and URANS." 17th Arizona Fluid Mechanics Conference, Tucson, AZ, February 9-10.

Wernz, S., and Fasel, H., 2001. "Numerical Investigation of Instability Mechanisms in Turbulent Wall Jets Using URANS." 54th Annual Meeting of the Division of Fluid Mechanics, San Diego, CA, November 18-20.

Wernz, S., Seidel, J., and Fasel, H., 2002. "Numerical Investigation of Turbulent Wall Jets." 40th AIAA Aerospace Sciences Meeting & Exhibit, Reno, NV, January 14-17.

# NUMERICAL INVESTIGATION OF TURBULENT WALL JETS

S. Wernz,* J. Seidel,† H. F. Fasel‡

Department of Aerospace and Mechanical Engineering, University of Arizona

Tucson, Arizona, USA

## Abstract

The evolution of large scale, coherent structures in turbulent wall jets is investigated numerically using our Flow Simulation Methodology (FSM). Previous experimental research has shown that these structures significantly change the mean Reynolds shear stress distribution and also the skin friction. The combination of the coherent motion in the shear layer region of the wall jet and the turbulent boundary layer underneath pose a unique challenge for turbulent simulations. We use FSM to investigate the effect of these large coherent structures, both in the unsteady Reynolds Averaged Navier-Stokes (URANS) limit and in the Large Eddy Simulations (LES) range. In addition, Direct Numerical Simulations (DNS) will be used to show the emergence of large structures with strong spanwise coherence during wall jet transition. The computational results are scrutinized to investigate the applicability and performance of FSM for this complex turbulent flow.

## 1  Introduction

A wall jet develops when a fluid is blown tangentially along a surface. Wall jets have many important technical applications such as boundary layer control and lift enhancement on airfoils, making use of their tendency to adhere to curved surfaces (Coanda effect). In other applications, such as the cooling of turbine blades and combustion chamber walls, a wall jet is used to cool and protect surfaces from hot and/or corrosive fluids. Despite its applications in many technical systems, the wall jet,

especially the role of large coherent structures in the turbulent wall jet, is not well understood.

With respect to numerical simulations, the turbulent wall jet is an ideal test case for turbulence models, since it combines two of the most studied flows: the turbulent wall boundary layer and the free shear layer. However, as was recognized early on [1], the interaction between these two prototypical flows is very important and needs to be modeled correctly to obtain results that match experimental findings.

A large number of experimental investigations of the mean flow of turbulent wall jets has been reported in the literature (see review articles [2], [1], [3]). Although the measurements are very consistent in a large portion of the mean profiles, the velocity in the near wall region is extraordinarily difficult to measure and therefore skin friction data vary considerably. The most important parameters describing a wall jet are its local velocity maximum, $U_m$, the wall normal location where it occurs, $y_m$, and the half width, $y_{0.5}$, which is the wall normal distance where the velocity has decayed to one half the local maximum. It is important to note that in the turbulent case, $y_m \approx 0.15 y_{0.5}$, and the edge of the jet is around $3 y_{0.5}$. This large discrepancy in length scales of the inner boundary layer region and the outer shear layer region poses unique challenges, both experimentally and numerically.

Since experimental investigations almost exclusively focused on the mean flow quantities, the question of the existence and influence of large coherent structures in the outer shear layer on the mean flow profiles was not addressed. From a hydrodynamic stability point of view, the shear layer region could be unstable to disturbances due to the inflection point in the mean velocity profile. This notion was investigated experimentally by Katz and coworkers [4], who have shown that large coherent structures do exist in the turbulent wall jet, and although these structures are visible mainly in the outer region of

---

*Research Associate.

†Assistant Research Professor. Member AIAA.

‡Professor, Aerospace and Mechanical Engineering. Member AIAA.

the wall jet, they profoundly change the whole flow field, as indicated by the significant change in the mean skin friction. More importantly, deliberately introducing these structures using periodic forcing results in predictable changes of the mean flow.

While there is an abundance of experimental data of turbulent wall jets, numerical simulations have only recently been reported ([5], [6], [7]). The difficulties in computing the turbulent wall jet can be traced back to the discrepancy of length scales between the boundary layer and the shear layer regions. In the computations, the near wall resolution required to resolve the steep gradients, combined with the large domain height necessary to accomodate the outer shear layer part makes this flow exceptionally challenging to compute, even if a turbulence model is used.

Most numerical investigations to date have focused on the mean flow quantities, using various turbulence models. The results presented in [4], however, indicate that the unsteady coherent motion strongly influences the mean flow of the turbulent wall jet. In addition, if the coherent motion is a result of a local flow instability, then steady turbulent simulations are unlikely to capture the relevant physics correctly. Therefore, in order to understand these physical mechanisms, an unsteady simulation spanning many eddy turnover times of the large coherent motion is necessary; at the same time, the simulation has to be accurate enough to account for the random turbulent motion.

To overcome the computational challenges described above, various techniques have been developed. Extending the success of Direct Numerical Simulation (DNS) from the laminar regime into the turbulent regime proved to be very instructive for understanding the relevant physical mechanisms in prototypical turbulent flows like the boundary layer or the free shear layer. However, when the Reynolds number is increased, these simulations quickly become too expensive even for todays supercomputers.

A different technique, based on approximating the turbulent mean flow, is Reynolds-averaged Navier-Stokes (RANS) simulation. RANS has long been used in industrial applications with good success. Unfortunately, RANS cannot, at least in its original form, account for flow unsteadiness and is therefore limited in its applicability to flows where

large, coherent (as opposed to random) motion is not important. But RANS is still the method of choice for simulating wall bounded shear flows for most practical applications.

Large Eddy Simulation (LES), as a third approach, is able to compute the unsteady, turbulent motion, and LES has become the method of choice in research for flows where the intricate turbulent flows physics are being investigated. Unfortunately, despite extensive research, LES could not live up to its claim to be a method capable of computing all turbulent flows. For a discussion of the shortcomings of LES, see ([8], [9], [10]).

More recently, efforts have been initiated to combine the strengths of these methods into a unified simulation strategy, sometimes refered to as hybrid models. An example is the Detached Eddy Simulation (DES) [11]. In principle, DES is a two layer model, combining the Spalart-Almaras turbulence model in the near wall region with a traditional LES away from the wall. The switch-over point is chosen in a rather ad hoc fashion, which is not critical if large coherent motion is being investigated away from the wall (like in wake flow simulations), but unphysical inconsistencies can be introduced if the switch-over point is not chosen carefully.

Our Flow Simulation Methodology (FSM), which we have been developing (originally in collaboration with C. Speziale [9], on the other hand, combines DNS, LES, and RANS in a consistent manner by using the same underlying turbulence model for the RANS and the LES part and all regimes between RANS and LES (e.g. [12]). In fact, FSM maintains the general form of LES, i.e., the large scales are computed and the small scales are modeled. The main feature of our FSM is that the subgrid-scale stress model of LES is replaced by the product of a contribution function and a state-of-the-art algebraic Reynolds stress model. The contribution function is designed such that, depending on a 'physical' numerical resolution (obtained by comparing the grid size to a relevant physical length scale, e.g., the Kolmogorov length scale), the simulations approach a DNS in the limit of fine resolution (or low Reynolds number), or an unsteady RANS in the limit of coarse resolution (or high Reynolds number).

In this paper, our Flow Simulation Methodology (FSM) is used to investigate the origin and

the role of the large coherent structures in wall jets. FSM has been developed because of the limitations in traditional computational strategies such as Direct Numerical Simulation (DNS), Reynolds-averaged Navier-Stokes (RANS) computation, and Large Eddy Simulation (LES).

# 2 Numerical Method

## 2.1 Governing Equations

The governing equations are the three–dimensional, incompressible, unsteady Navier–Stokes equations in vorticity-velocity formulation. The velocity components in the streamwise ($x$), wall normal ($y$), and spanwise ($z$) directions are $u$, $v$, and $w$, respectively (figure 1).

In these equations, the velocities are normalized by the jet exit velocity $U_j$, the spatial variables $x, y, z$ by the nozzle width $b$, and the time by $b/U_j$. Taking the curl of the momentum equations, which eliminates the pressure gradient terms, yields the transport equations for the vorticity,

$$\frac{\partial \vec{\omega}}{\partial t} + \nabla \times \left( \vec{\omega} \times \vec{V} - \nabla \cdot \vec{\bar{\tau}} \right) = \frac{1}{Re_j} \nabla^2 \vec{\omega}, \quad (1)$$

For simulations using a turbulence model, $\vec{\bar{\tau}} = [\tau_{ij}]$ is the turbulent stress tensor. In the two-dimensional case, this set of equations reduces to one equation for the spanwise vorticity component $\omega_z$. The velocity components are computed from a set of Poisson equations (see [13] for more details).

In order to close equation (1) for turbulent simulations, the turbulent stress tensor components $\tau_{ij}$ need to be modeled. The model used in this investigation is our new FSM. Following Speziale [9], the turbulent stress tensor components are written as

$$\tau_{ij} = f(\Delta/L_k)\tau_{ij}^R, \quad (2)$$

where $\tau_{ij}^R$ is the Reynolds stress tensor and $f(\Delta/L_k)$ is the contribution function,

$$f(\Delta/L_k) = [1 - \exp(-5 \max(0, \Delta - 2L_k)/NL_k)]^n. \quad (3)$$

$\Delta$ is the effective computational grid size, $L_k = \left(\nu^3/\epsilon\right)^{1/4}$ is the Kolmogorov length scale, and $N$ and $n$ (in this study $n = 1$) are model constants.

Note that the contribution function depends on the ratio $(\Delta/L_k)$, i.e., the physical resolution of the computation compared to a length scale of turbulence in the flow. It should be pointed out that physically relevant length scales other than $L_k$ can be chosen, e.g., an estimate of the integral length [14]. The Reynolds stress $\tau_{ij}^R$ in equation (2) is computed using the anisotropic Algebraic Stress Model (ASM) of Gatski and Speziale [15],

$$\begin{aligned}
\tau_{ij}^R = \ & \frac{2}{3}K\delta_{ij} \\
& -f(\eta,\xi)\left[ \alpha_1 \frac{k^2}{\epsilon}\overline{S}_{ij} \right. \\
& \left. +\alpha_2 \frac{k^3}{\epsilon^2}\left( \overline{S}_{ik}\overline{W}_{kj} + \overline{S}_{jk}\overline{W}_{ki} \right) \right. \\
& \left. -\alpha_3 \frac{k^3}{\epsilon^2}\left( \overline{S}_{ik}\overline{S}_{kj} - \frac{1}{3}\overline{S}_{kl}\overline{S}_{kl}\delta_{ij} \right) \right]. \quad (4)
\end{aligned}$$

The strain rate tensor and vorticity tensor are given by

$$\overline{S}_{ij} = \frac{1}{2}\left( \frac{\partial \overline{u}_i}{\partial x_j} + \frac{\partial \overline{u}_j}{\partial x_i} \right), \overline{W}_{ij} = \frac{1}{2}\left( \frac{\partial \overline{u}_i}{\partial x_j} - \frac{\partial \overline{u}_j}{\partial x_i} \right). \quad (5)$$

The function $f(\eta,\xi)$, in conjunction with $k^2/\epsilon$, assumes the role of a nonlinear eddy viscosity, and is given by

$$f(\eta,\xi) = \frac{3}{3 - 2\eta^2 + 6\xi^2} \approx \frac{3(1 + \eta^2)}{3 + \eta^2 + 6\eta^2\xi^2 + 6\xi^2}, \quad (6)$$

where the expression on the right hand side of equation 6 is a regularized form of $f(\eta,\xi)$, which is used to avoid a possible division by zero in the original expression [9].

$\eta$ and $\xi$ are invariants of the irrotational strain rate tensor and the vorticity tensor, respectively,

$$\eta = \frac{1}{2}\frac{\alpha_3}{\alpha_1}\frac{k}{\epsilon}\left( \overline{S}_{ij}\overline{S}_{ij} \right)^{1/2}, \xi = \frac{\alpha_2}{\alpha_1}\frac{k}{\epsilon}\left( \overline{W}_{ij}\overline{W}_{ij} \right)^{1/2}. \quad (7)$$

The values of model constants in equations (4) and (7) are $\alpha_1 = 0.227$, $\alpha_2 = 0.0423$, and $\alpha_3 = 0.0396$.

The turbulent kinetic energy $k$ and the turbulent dissipation rate $\epsilon$ in equation (4) are computed from the standard transport equations [16],

$$\frac{Dk}{Dt} = -\tau_{ij}\frac{\partial \overline{u}_i}{\partial x_j} - \epsilon + \frac{\partial}{\partial x_j}\left[ \left( \frac{\nu_T}{\sigma_k} + \frac{1}{Re} \right) \frac{\partial k}{\partial x_j} \right] \quad (8)$$
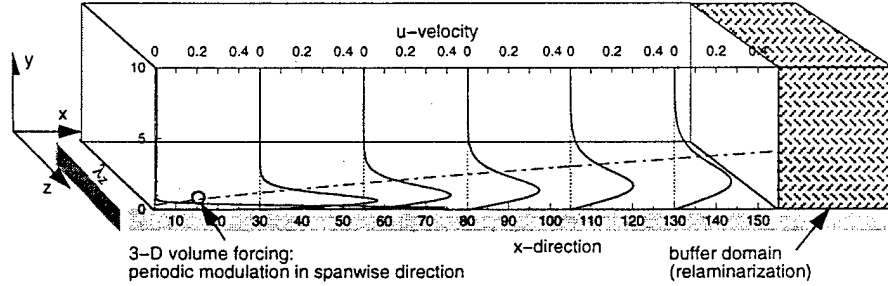
Figure 1: Computational domain with schematic of volume forcing for disturbance generation.

$$\frac{D\epsilon}{Dt} = -C_{\epsilon 1}\frac{\epsilon}{k}\tau_{ij}\frac{\partial \overline{u}_i}{\partial x_j} - C_{\epsilon 2}f_{\epsilon 2}\frac{\epsilon^2}{k}$$
$$+ \frac{\partial}{\partial x_j}\left[\left(\frac{\nu_T}{\sigma_\epsilon} + \frac{1}{Re}\right)\frac{\partial \epsilon}{\partial x_j}\right] . \quad (9)$$

The eddy-viscosity $\nu_T$ and the wall damping function $f_{\epsilon_2}$ are defined as

$$\nu_T = C_\mu k^2/\epsilon, \quad f_{\epsilon 2} = 1 - e^{-y\,Re\sqrt{k}/10} . \quad (10)$$

Finally, the constants needed for the solution of equations (8) through (10) are,

$$C_\mu = 0.09, \quad C_{\epsilon 1} = 1.44, \quad C_{\epsilon 2} = 1.83,$$
$$\sigma_k = 1, \quad \sigma_\epsilon = 1.3, \quad A^+ = 25.$$

## 2.2 Numerical Scheme

A detailed description of the numerical schemes used for the solution of equation (1) and the Poisson equations for the velocities is given in [13]. For the time integration, a fourth-order accurate explicit Runge-Kutta method is used. The derivatives in the streamwise direction are approximated by fourth-order compact upwind and downwind biased differences at consecutive time steps and wall-normal derivatives are computed with fourth-order accurate compact differences. In the spanwise direction, a pseudospectral approach is used. Lastly, a fast Fourier solver is implemented for the solution of the velocity Poisson equations.

In addition to the solution of the vorticity transport equation and the velocity Poisson equations, FSM requires the simultaneous integration of the $k$ and $\epsilon$ equations. For these equations, a second order ADI method is used for the time integration and

second-order accurate difference stencils are employed for the streamwise and wall normal derivatives. The fourth-order accurate difference method used in the discretization of the vorticity transport equation is employed for the spatial derivatives of the turbulent stress tensor components (see equation (1)).

## 2.3 Initial and Boundary Conditions

The governing equations are solved in the computational domain shown in figure 1. At the inflow boundary, Dirichlet conditions are imposed for the vorticity, the velocity components, the turbulent kinetic energy, and the turbulent dissipation rate. For the computations presented here, the inflow conditions are obtained from a solution of the boundary layer equations for the turbulent wall jet. At the wall $y = 0$, the no-slip, no-penetration conditions are imposed on the velocity. The turbulent kinetic energy is set to zero, and a Neumann condition is used for the turbulent dissipation rate. At the free stream boundary $y = y_{max}$, a decay condition is imposed on v, and the wall normal derivative is set to zero for all other quantities. This requires the domain height to be large enough so that all disturbances have decayed sufficiently and the imposed boundary conditions do not influence the solution. Near the outflow boundary, a damping region similar to the one proposed by [17] is used. At the outflow boundary itself, all second derivatives are set to zero.

As initial condition, the vorticity and velocity components are prescribed. The turbulent kinetic energy $k$ and the turbulent dissipation rate $\epsilon$ are prescribed in addition. For the turbulent simulations (RANS and URANS), these quantities are

obtained from the solution of the boundary layer equations for the turbulent wall jet, otherwise, the inflow boundary condition and the initial condition are obtained from the Glauert similarity solution.

Disturbances are introduced into the flow using a volume forcing technique [21]. With this method, predominantly vortical disturbances can be generated anywhere in the flow field. In the cases presented in this paper, the volume forcing is applied near the inflow boundary.

# 3   Results

## 3.1   Unsteady Reynolds Averaged Navier-Stokes Simulations

Two-dimensional computations of the mean flow of the turbulent wall jet are used to validate our new FSM in the limit of traditional (steady) RANS. These computations have been described in detail in [7] and are not shown here.

Very good agreement was achieved between experimental findings and the computational results. However, some of the shortcomings of steady turbulent simulations became apparent. First, although anisotropic effects are included in the model, the distribution of the streamwise Reynolds stress $R_{11}$ showed considerable deviations in the near wall region. Second, we found that the non-equilibrium nature of the turbulent wall jet cannot be captured with an ASM model of the form of equation (4) (or any other equilibrium $k - \epsilon$ model).

### 3.1.1   Effect of forcing on the turbulent wall jet

Using the Flow Simulation Methodology (FSM) in the unsteady RANS limit, the effect of large coherent structures on the turbulent wall jet was investigated. Even though FSM was developed to be used as a subgrid scale turbulence model, it is of particular importance that computations in the unsteady RANS limit yield accurate results. The disturbances are introduced into the turbulent base flow using the volume forcing method described in section 2.3.

For comparison, experiments with periodic forcing by Katz et al. [4] are used. They achieve a skin friction reduction on the order of 10% with a
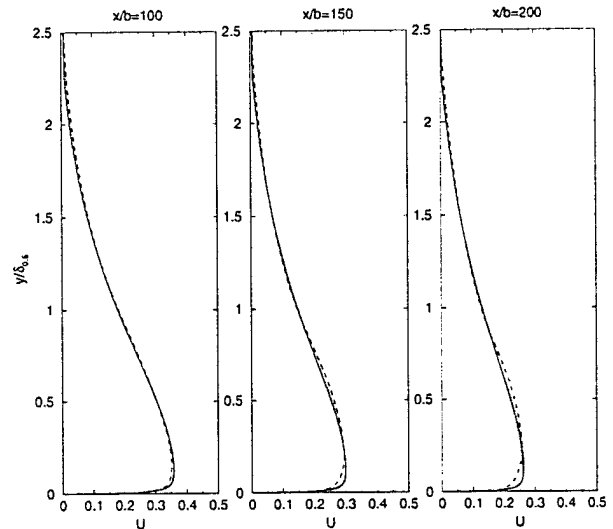


Figure 2: Effect of large scale structures on the mean $u$-velocity profile. —— Base Flow, $\cdots$ Case02, – – – Case03.

forcing amplitude of only 5%. From the large coherent structures observed in a flow visualization, they concluded that these structures result from an instability of the turbulent wall jet. They also showed that the natural unforced turbulent wall jet has a strong spanwise coherence, which is increased considerably by periodic forcing. If these coherent structures are in fact nearly two-dimensional, a two-dimensional simulation should be sufficient to model the effect of periodic forcing on the large coherent structures, and as a consequence, on the mean flow of the turbulent wall jet.

The forcing frequency was chosen at $f = 17$ Hz. In table 1, the forcing amplitudes for the cases described in the following are summarized. Figure 2 compares the mean flow profiles of Case02 and Case03 with the profile of the undisturbed base flow at $x/b = 100, 150, 200$ ($b$ is the nozzle height). In Case03, the large forcing amplitudes cause a significant mean flow distortion. Note that this mean flow distortion increases in streamwise direction, indicating that the disturbances in the flow actually enable a momentum transfer from the mean flow to the large, coherent structures.

To illustrate how the large, coherent structures influence the mean flow, the Reynolds shear stress contribution of the coherent motion, $\overline{u'v'}_c$, the

| Case | Case01 | Case02 | Case03 |
|------|--------|--------|--------|
| $\hat{f}/U_j$ | $5 \times 10^{-3}$ | $1 \times 10^{-2}$ | $2 \times 10^{-2}$ |

Table 1: Disturbance amplitudes for URANS simulations.

Reynolds stress of the modeled small scales, $R_{12}$, and the sum $\overline{u'v'}_c + R_{12}$ for Case03 are plotted in figure 3 as a function of the wall normal distance. The results show that the large scale structures increase the Reynolds stress from very close to the wall to about the wall jet half width and have very little effect in the outer part of the shear layer. As can be seen from the figure, this also means that the $y$ location of the zero of the Reynolds stress is now displaced from the location of the velocity maximum towards the wall. The displacement is in surprisingly good agreement with experimental findings ($y_{R_{12}=0} \approx 0.6 y_{1/2}$ at $x/b = 200$). This shift has so far been attributed to nonequilibrium effects and its origin and importance has been the subject of considerable controversy. The simulations presented here indicate that the large unsteady shear layer structures, in conjunction with their nonlinearly created harmonics, are a major contributor to this effect. Figure 4 compares $R_{12}$ from the ASM model without large scale structures, the sum $\overline{u'v'}_c + R_{12}$, and experimental results of Eriksson *et al.* [19].

In summary, ASM in the limit of unsteady RANS can capture the effect of the large coherent motion. However, these structures have to be introduced into the flow by—in this case—periodic blowing and suction because unsteady RANS is unsuitable for a computation through transition.

## 3.2 Direct Numerical Simulations

While many experimental findings are matched remarkably well by our URANS calculations (f=1 in eqn. 2), some considerable differences have become apparent as well. Firstly, the fully developed turbulent flow in the URANS calculations is far less receptive to forcing than the transitional region close to the nozzle where forcing occurs in experiments. As a result, very large forcing amplitudes are required for producing large amplitude disturbances and numerical instabilities (due to the turbulence
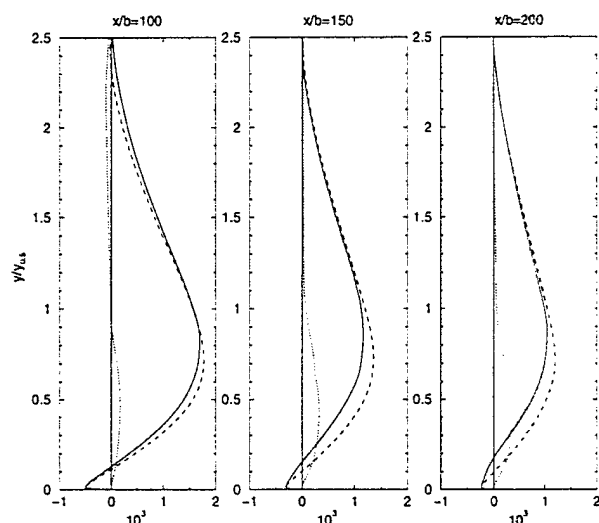


Figure 3: Reynolds stresss $R_{12}$. —— random part (modeled), $\cdots$ coherent part, – – – sum of coherent and random parts.
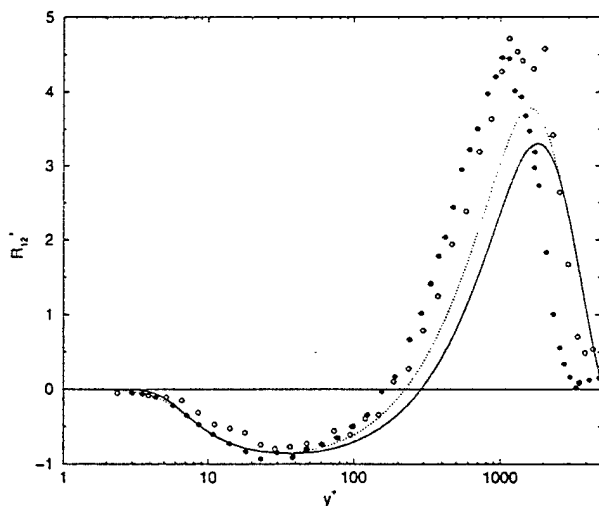


Figure 4: Reynolds stresss $R_{12}$ in inner coordinates. —— Mean flow without large structures, $\cdots$ Mean flow with large structures. o experimental results at $x/b = 70$, • at $x/b = 150$ [19].

model) limit the achievable disturbance amplitude. Secondly, in URANS calculations the generated disturbances are mostly damped rather than amplified. This is in contrast to the experimental results by Katz et al. [4], who reported significant disturbance

growth in the fully developed turbulent wall jet. On the other hand, Schober [20] concluded from his experiments that 2D coherent structures in the turbulent wall jet are damped rather than amplified. In his view these structures are remnants of disturbances originating from the narrow shear layer upstream at the upper nozzle lip, where the flow is still transitional.

To address these issues we have performed Direct Numerical Simulations (DNS) of a high momentum wall jet through transition into the turbulent regime (for details see [21]). In these simulations, a laminar Glauert wall jet ($Re_{\delta 0.5} = 16,500$ at the inflow) is perturbed by volume forcing with several (incommensurate) frequencies and with large amplitudes. The laminar wall jet is perturbed close to the inflow at the most receptive wall-normal locations in both the inner and the outer flow regions. Although the forcing is applied in higher spanwise modes, i.e., no two-dimensional wave component is introduced, the simulations show the emergence of large structures with a very strong spanwise coherence. This clearly indicates that the wall jet naturally supports these structures. From a hydrodynamic stability point of view, these structures could be connected to an inflectional instability of the outer shear layer region of the wall jet. These findings are in good qualitative agreement with results from [20], although his experimental setup is quite different from our simulations. A snapshot of the flow field is shown in figure 5, where the isolevels of spanwise vorticity are shown in a perspective view in the computational domain.

To determine the quality of the turbulent flow computed with the DNS, characteristic time-averaged flow quantities at several streamwise locations have been compared with experimental measurements [19]. In figure 6, a comparison for the streamwise mean velocity and the Reynolds shear stress is shown in inner and in outer coordinates. Except for the first and last streamwise station, which are too close to the forcing location and the buffer domain respectively, the velocity and shear stress profiles match the experimental data quite well. The agreement is, in fact, far better than in any previous attempt at computing a fully turbulent wall jet using DNS, particularly for $y^+ < 100$ in inner coordinates. Interestingly, the streamwise velocity in figure 6a exhibits an apparent log-

layer which is much more pronounced and closer to the experimental data than for RANS calculations. However, the location of the streamwise velocity maximum in the DNS is farther away from the wall than in the experiment. The reason for this might be that the 2D coherent structures are somewhat more intense in the DNS than in the experiment (and in our URANS calculations), which, in turn, may be caused by insufficient grid resolution, particularly in the outer region close to the edge of the wall jet.

In summary, the DNS has shown that coherent structures are generated during transitions and that these structures persist in the turbulent flow regime. It was also shown that the mean flow data from the DNS are quite close to turbulent wall jet mean flow data obtained from experiments and RANS calculations. The agreement is especially when considering that the laminar Glauert wall jet used as inflow and initial condition exhibits a vastly different shape and streamwise development. The goal for our FSM investigation is to explore to what extend comparable results can be obtained on a coarser computational grid.

## 3.3 Flow Simulation Methodology

Extensive investigations of the FSM have been performed for a zero pressure gradient, flat plate boundary layer [12] and good agreement with the theoretical predictions and other (well resolved) LES and DNS simulations was found. However, for wall jets, our FSM calculations in the range of LES are still at a preliminary stage. We have chosen the contribution function suggested in [12] (eqn. 3). Here, a case study will be presented to demonstrate the performance of FSM throughout its range from a DNS with $f(\Delta, L_k) = 0$ (Case F1) to URANS with $f(\Delta, L_k) = 1$ (Case F5). Case F1 represents the DNS discussed above and serves as a reference. Cases F2-F5 employ the DNS as an initial condition and use the same computational setup (computational domain, inflow condition and forcing). However, in these cases, the turbulence model is ramped in between $x = 10$ and $x = 20$ where the flow transitions to turbulence. The computational parameters for the five cases are summarized in table 2. In Case F2, which has the identical computational grid as the DNS, the FSM is performed in the

filtered $\omega_z$-vorticity

$\omega_z$=-1 (ccw)
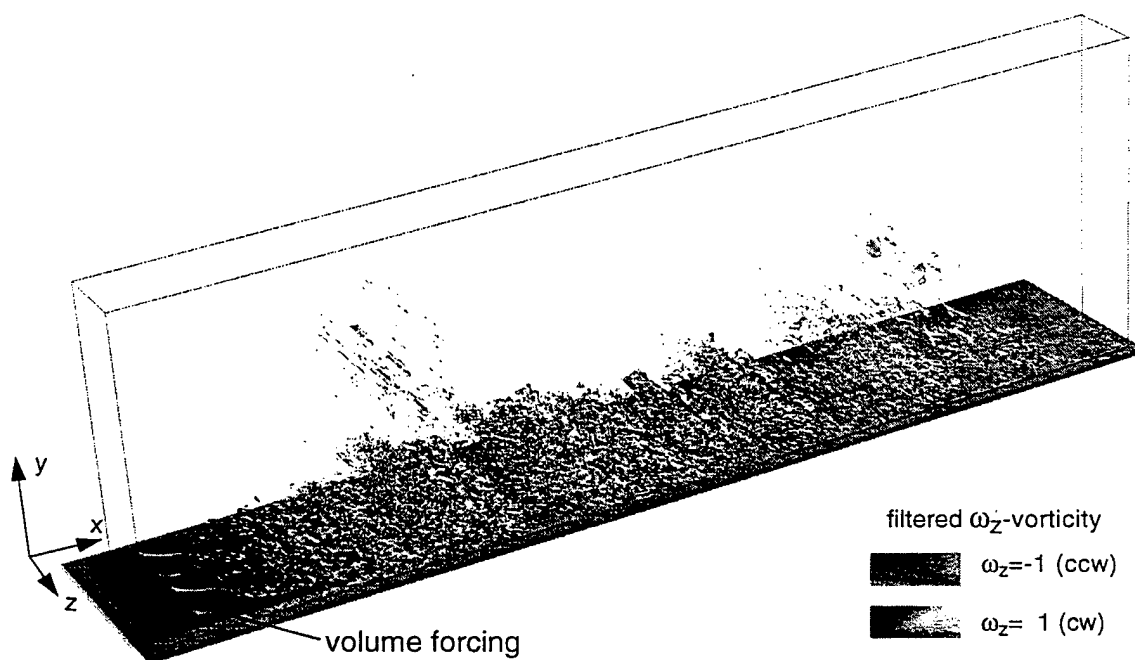
$\omega_z$= 1 (cw)

volume forcing

Figure 5: Direct Numerical Simulation of wall jet transition. Isolevels of spanwise vorticity.

regime where the model contribution is quite small. Here, the turbulence model mainly serves to reduce gridmesh oscillations that are prevalent in the DNS as the resolution in the DNS is not quite sufficient. Cases F3 and F4, both on coarser grids, are designed to have virtually all small scales modeled but without the strong damping effect of the model on the larger scales as in the URANS limit. Figure 7 compares the level of the model contribution for the five cases at one time instant, $t = 2/34Hz$. Shown are the values of the contribution functions at the wall which are obtained by multiplying by an artificial ramp function (e.g., see figure 7, Case F5). Upstream of $x = 10$, the model is shut off in all cases.

Results from the case study are presented in figures 8-10. An impression of the flow fields corresponding to all five cases is provided with the isolevel plots in figure 8, which display the spanwise average of the instantaneous spanwise vorticity. For Case F1 (figure 8a), the flow exhibits small scale structures embedded in the large 2D structures throughout the computational domain. The large, coherent structures consist of counter-rotating vortex pairs corresponding to the inner and

the outer flow regions of the wall jet. At $x = 45$, several vortices are in the process of merging and lifting away from the wall.

For Cases F2-F4, at the time instant shown ($t = 2/34Hz$), the flow adjustment following the introduction of the turbulence model at $t = 1/34Hz$ is completed. For the LES in figure 8b the smaller scales are reduced, yet the large scale structures still correlate well with those in the DNS. The structure at $x = 45$ is somewhat enhanced and in the process of lifting off from the wall. This lift-off of dipolar vortices by mutual induction is a very common phenomenon in laminar wall jets [22]. In the turbulent flow, however, the near wall vortex is usually too weak to propel the pair away from the wall jet core. With the contribution of the turbulence model, the subgrid scale stress replaces the weakening effect of the small scale structures on the large structures. Indeed, while the dipolar structure is even more pronounced in Case F3 (figure 8c), it is not strong enough to lift away from the wall. Interestingly, the lift-off process does not occur for Case F4 (figure 8d), which has a very coarse spanwise resolution. In both Cases F3 and F4, the smaller structures are mostly confined to the outer edge of the wall

a) streamwise velocity in inner coordinates

b) streamwise velocity in outer coordinates

c) Reynolds stress in inner coordinates
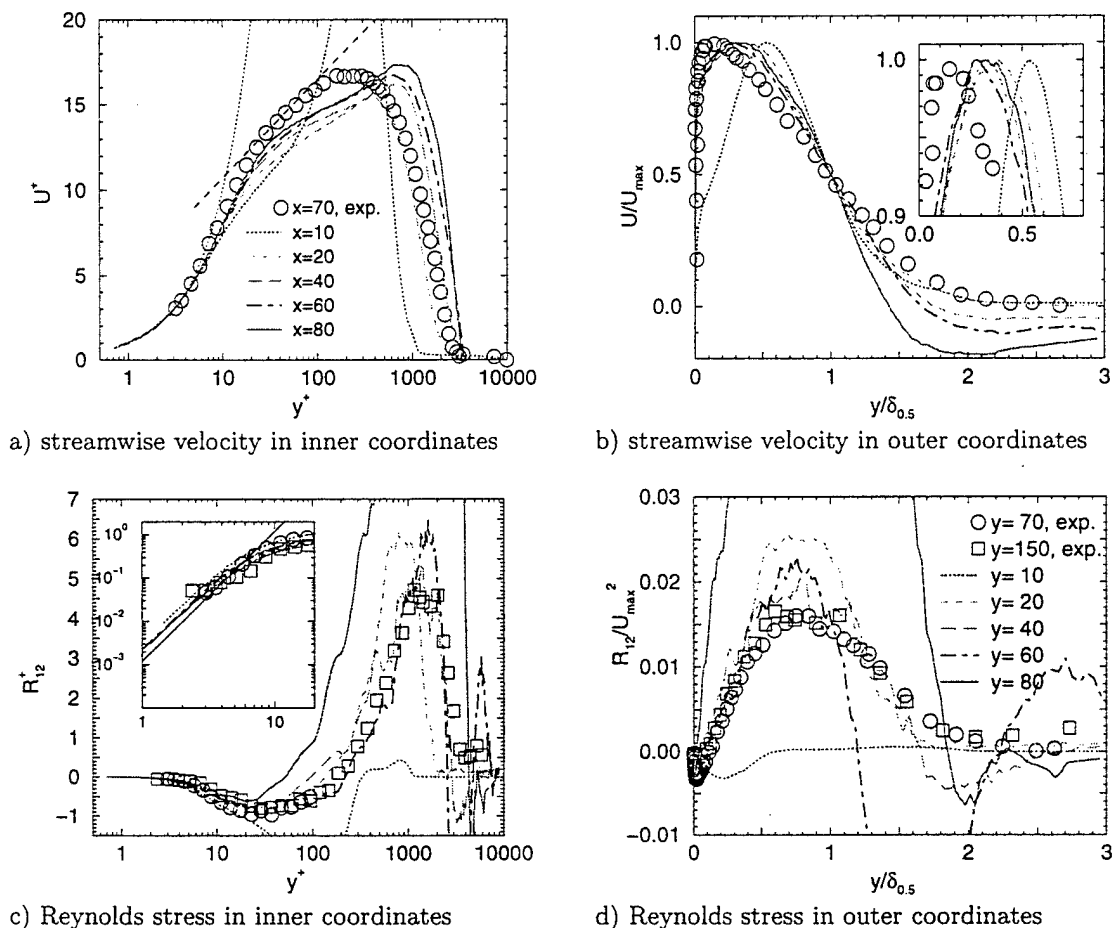
d) Reynolds stress in outer coordinates

Figure 6: Time-averaged flow from a DNS of bypass transition in the high Reynolds number wall jet. Shown for comparison are measurements at $x = 70$ from experiments by [19].

jet where the contribution function shuts down the model as $L_k$ increases. Still, size and spacing of the large structures is approximately preserved. This is clearly not the case for the URANS in Case F5 (figure 8e). With the contribution function $f = 1$, the formation of the large 2D structures from 3D disturbances is suppressed and their intensity is too small to be visible in the plot.

The increased two-dimensionality of the coherent structures with increased model contribution is illustrated in figure 9. Shown are isolevels of spanwise vorticity on the wall ($y = 0$). For Case F1 (figure 9a) the 2D structures are strongly modulated by 3D disturbances. This modulation is much weaker

for Case F2 (figure 9b) where the small scales are reduced in amplitude due to the model. For cases F3 & F4 (figures 9c&d), the modulation is hardly visible and for Case F5 (figure 9e) all structures are suppressed once the model is fully turned on ($f = 1$).

The temporal development of the 2D coherent structures in is illustrated in the space-time diagrams of spanwise wall vorticity of figure 10 for cases F1-F4. The overall pattern of the time-traces for the vortical structures is similar in all cases, i.e., the spacing (or wave length) of the disturbances increases in streamwise direction as the wall jet spreads. The most pronounced difference is the wall

9

| Case | F1 | F2 | F3 | F4 | F5 |
|------|-----|-----|--------|--------|--------|
| Type | DNS | LES | coarse LES | coarse LES | URANS |
| $N$ | $\infty$ | 2500 | 1000 | 1500 | 0 |
| $\Delta x[5mm]$ | 0.1 | 0.1 | 0.2 | 0.2 | 0.2 |
| $\Delta z[5mm]$ | 0.05 | 0.05 | 0.1 | 0.25 | 0.1 |
| $i$ | 801 | 801 | 401 | 401 | 401 |
| $k$ | 21 | 21 | 11 | 5 | 11 |

Table 2: Model parameter and resolution for FSM cases.



Figure 7: Wall values of the contribution functions for Cases F1-F5.

signature of the lift-off of the vortical structures in the Cases F2 & F3 (figures 9b &c), which leaves wedge-like voids in the pattern.

The effect for Cases F1-F5 of the turbulence model on the mean flow is illustrated in figure 11 which shows the streamwise mean velocity in inner coordinates. The observed trends are extremely encouraging. The velocity maximum shifts back towards the experimental measurement curve as the model contribution is increased from case to case. Cases F2-F4 exhibit the "log-like" layer which is measured experimentally and cannot be captured by conventional RANS calculations. The curves for Cases F3 & F4 are very close to each other despite the difference in spanwise resolution. Case F2 appears closest to the measurement data. It is unclear at this time what causes Cases F1-F4 containing time-dependent structures to narrow the peak at the velocity maximum. Possibly, the narrow width of the domain and/or the fact that only symmetric Fourier modes are computed might play a role. Alternaqtively the narrow peak may be an artifact of the rapid, bypass-type transition process caused by the large amplitude forcing. A more detailed analysis of the present results and further investigations with parameter studies will be needed.

## 4 Concluding Remarks

In this paper, the development of large, coherent structures and their effect on the mean flow of a turbulent wall jet has been investigated with our new Flow Simulation Methodology (FSM). FSM combines a state-of-the-art algebraic stress model (ASM) with a contribution function $f(\Delta, L_k)$ and presents a unified approach to computing turbulent flows, spanning the range from DNS to RANS. The contribution function determines the appropriate amount of modeling according to the physical resolution of the simulation by comparing the local grid spacing with a local, instantaneous turbulent length scale. For the investigations presented here, FSM was used in the limit of unsteady RANS ($f = 1$), in the limit of DNS ($f = 0$), and for two levels of modeling contribution, an LES and a coarse LES.
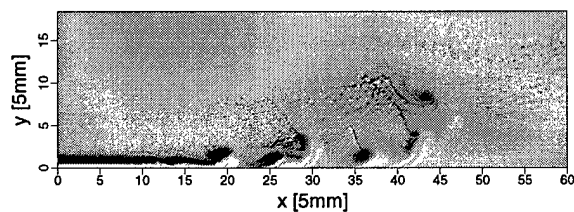
Without adapting the underlying ASM model or contribution function to the wall jet flow, the wall jet mean flow as well as the evolution of the large coherent structures observed experimentally are captured using FSM, and many interesting features of this complex turbulent flow are preserved. Examples include the displacement of the location of zero Reynolds shear stress from the location of maximum velocity (due to the coherent motion), merging of the vortical structures, and their occasional lift-off from the wall. More importantly, these intricate physical mechanisms are captured with a significantly reduced resolution. The results presented here show the applicability of the FSM approach for complex turbulent flow simulations.
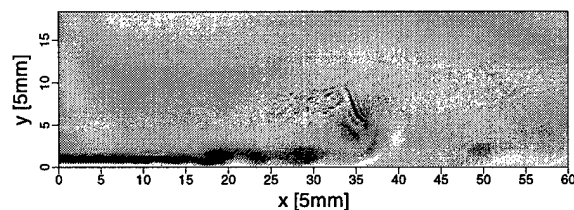
## Acknowledgement

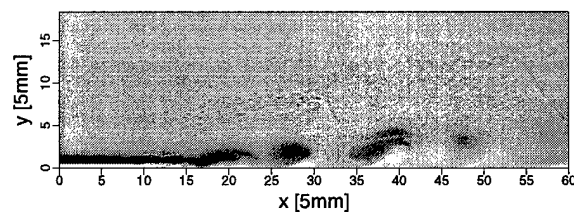a) Case F1 (DNS)

a) Case F1 (DNS)

b) Case F2 ("LES")
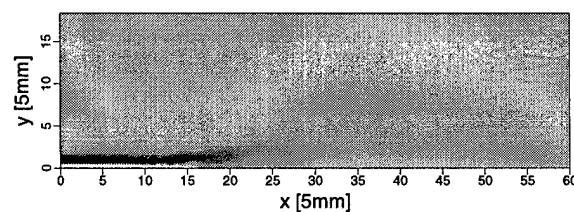
b) Case F2 ("LES")

c) Case F3 ("coarse LES")
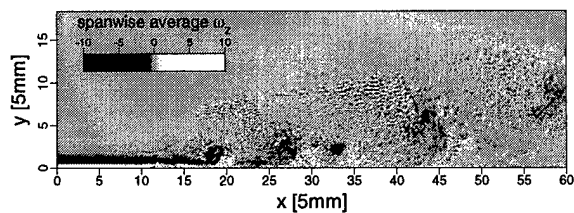
c) Case F3 ("coarse LES")

d) Case F4 ("coarse LES")

d) Case F4 ("coarse LES")

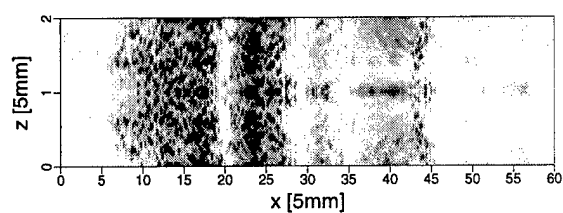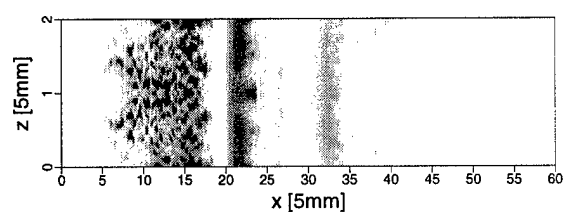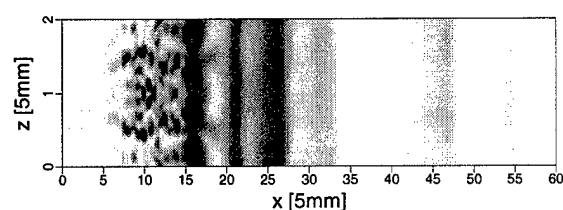e) Case F5 (URANS)

e) Case F5 (URANS)

Figure 8: Isolevels of instantaneous spanwise vorticity (spanwise average) from the FSM calculations (Case F1-F5) at time instant $t = 200/34Hz$.
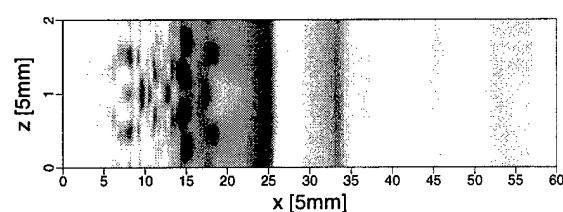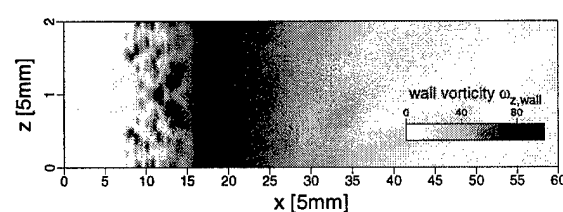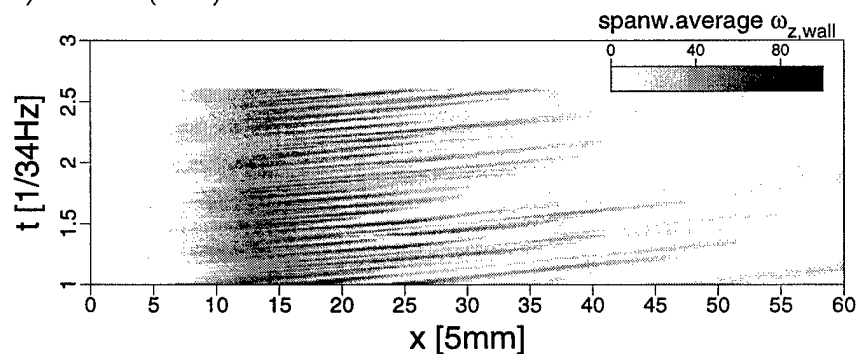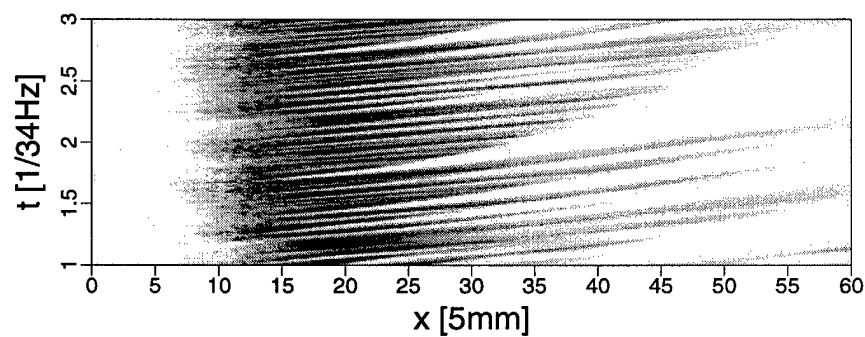
Figure 9: Instantaneous flow fields from the FSM calculations (Cases F1-F5) at time $t = 200/34Hz$. Shown are isolevels of spanwise wall vorticity.
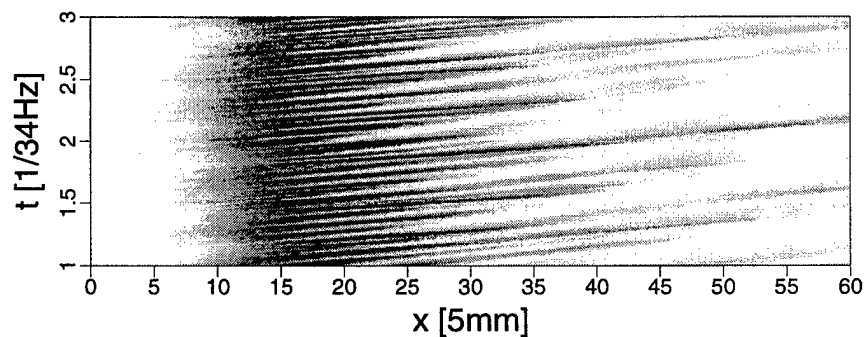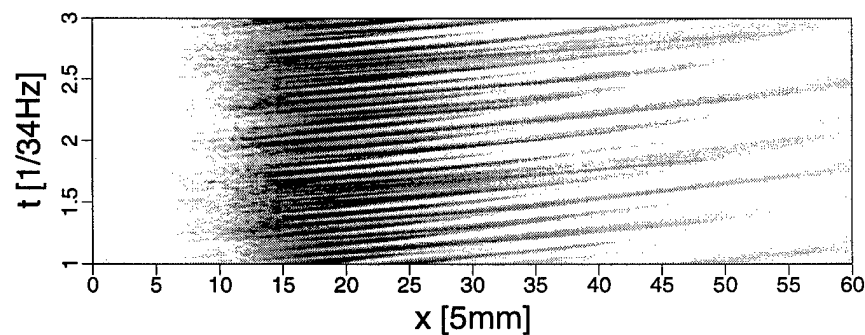
a) Case F1 (DNS)

b) Case F2 ("LES")

c) Case F3 ("coarse LES")

d) Case F4 ("coarse LES")

Figure 10: Space-time diagram of spanwise wall vorticity from the FSM calculations (Cases F1-F4) at time $t = 200/34Hz$.
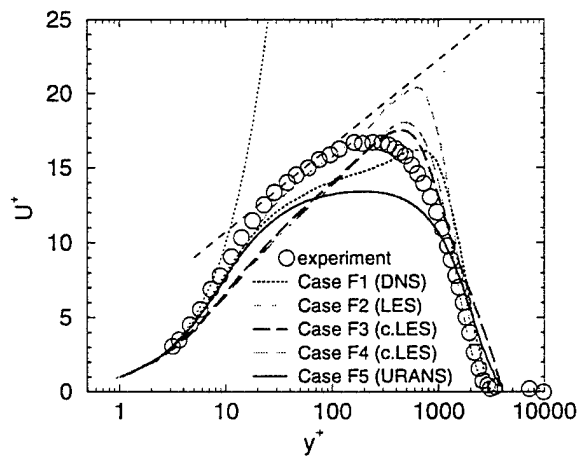
Figure 11: Mean streamwise velocity profiles from the FSM calculations (Cases F1-F5) in inner coordinates ($x = 40$). Shown for comparison are measurements at $x = 70$ from experiments [19].

# References

[1] B. E. Launder and W. Rodi. The turbulent wall jet — measurements and modeling. *Ann. Rev. Fluid Mech*, 15:429–459, 1983.

[2] B. E. Launder and W. Rodi. The turbulent wall jet. *Prog. Aerospace Sci.*, 19:81–128, 1981.

[3] M. E. Schneider and R. J. Goldstein. Laser doppler measurement of turbulence parameters in a two-dimensional plane wall jet. *Phys. Fluids*, 6(9):3116–3129, 1994.

[4] Y. Katz, E. Horev, and I Wygnanski. The forced turbulent wall jet. *J. Fluid Mech.*, 242:577–609, 1992.

[5] G. Gerodimos and R. M. C. So. Near-wall modeling of plane turbulent wall jets. *Journal of Fluids Engineering*, 119:304–313, 1997.

[6] H. I. Andersson, A. O. Braseth, and B. Holmedal. Computation of the inlet wall jet in a rectangular enclosure. *Comp. Fluid Dyn.*, 1:217–232, 1993.

[7] J. Seidel. *Numerical investigations of forced laminar and turbulent wall jets over a heated surface.* PhD thesis, The University of Arizona, 2000.

[8] B. Kosović. Subgrid-scale modelling for the large-eddy simulation of high-Reynolds-number boundary layers. *J. Fluid Mech.*, 336:151–182, 1997.

[9] C. G. Speziale. Turbulence modeling for time-dependent RANS and VLES: A review. *AIAA J.*, 26:173–184, 1998.

[10] J. Jiménez and R. D. Moser. LES: where are we and what can we expect. *AIAA Paper*, 98-2891, 1998.

[11] P. R. Spalart, Jou W.-H., M. Strelets, and S. R. Allmaras. Comments on the feasibility of LES for wings, and on a hybrid RANS/LES approach. In *Advances in DNS/LES, 1st AFOSR Int. Conf. on DNS/LES, Aug 4-8, 1997.* Greyden Press, Columbus, OH, 1997.

[12] H. L. Zhang, C. R. Bachman, and H. F. Fasel. Reynolds-Averaged Navier-Stokes calculations of unsteady turbulent flow. *AIAA Paper*, 2000-0143, 2000.

[13] H. Meitz and H. F. Fasel. A compact-difference scheme for the Navier-Stokes equations in vorticity-velocity formulation. *J. Comp. Phys.*, 157:371–403, 2000.

[14] D. Israel and H. Fasel. Numerical investigation of turbulent separation control using periodic disturbances. *AIAA Paper*, 2002-0409, 2002.

[15] T. B. Gatski and C. G. Speziale. On explicit algebraic stress models for complex turbulent flows. *J. Fluid Mech.*, 254:59–78, 1993.

[16] W. P. Jones and B. E. Launder. The prediction of laminarization with a two-equation model of turbulence. *Int. J. Heat Mass Transfer*, 15:301–314, 1972.

[17] M. Kloker, U. Konzelmann, and H. Fasel. Outflow boundary conditions for spatial Navier-Stokes simulations of transitional boundary layers. *AIAA J.*, 31 (4), 1993.

[18] H. Meitz. *Numerical investigation of suction in a transitional flat-plate boundary layer.* PhD thesis, The University of Arizona, 1996.

[19] J. G. Eriksson, R. I. Karlsson, and J. Persson. An experimental study of a two-dimensional plane turbulent wall jet. *Exp. Fluids*, 25:50–60, 1998.

[20] M. Schober. *Beeinflussung inkompressibler turbulenter Wandstrahlen*. PhD thesis, Technische Universität Berlin, 1999.

[21] S. Wernz. *Numerical investigation of forced transitional and turbulent wall jets*. PhD thesis, The University of Arizona, 2001.

[22] S. Wernz and H. F. Fasel. Numerical investigation of unsteady phenomena in wall jets. *AIAA Paper*, 96-0079, 1996.